

AD-A128 623

REVIEW OF TWO-STAGE FEL RESEARCH AT KMS FUSION(U) KMS
FUSION INC ANN ARBOR MI S B SEGALL ET AL. 21 JAN 83
KMSF-U1307 N00014-80-C-0614

1/1

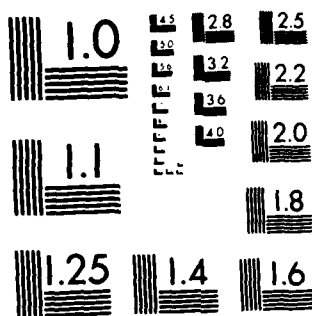
UNCLASSIFIED

F/G 20/5

NL



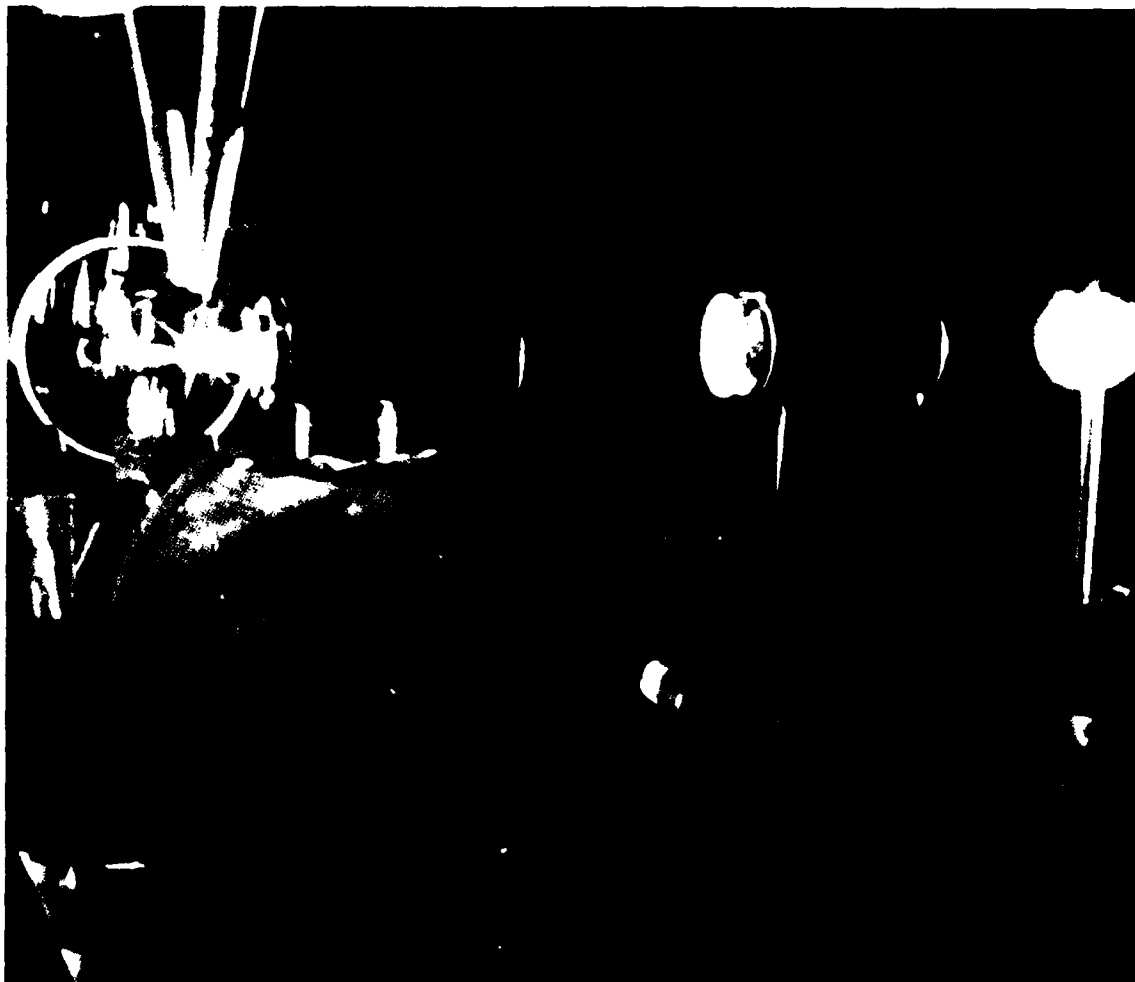
END
DATE
FILMED
6 83
DTIC



MICROCOPY RESOLUTION TEST CHART
NATIONAL BUREAU OF STANDARDS-1963-A

**.kms
fusion**
inc.

REVIEW OF TWO-STAGE FEL RESEARCH AT KMS FUSION
(JANUARY THROUGH SEPTEMBER, 1982)



DTIC FILE COPY

AD A128023

This document has been approved
for public release and sale; its
distribution is unlimited.

IC
MAY 1983

REPORT DOCUMENTATION PAGE		READ INSTRUCTIONS BEFORE COMPLETING FORM
1. REPORT NUMBER KMSF-U1307	2. GOVT ACCESSION NO.	3. RECIPIENT'S CATALOG NUMBER
4. TITLE (and Subtitle) Review of Two-Stage FEL Research at KMS Fusion (January through September, 1982)		5. TYPE OF REPORT & PERIOD COVERED Technical Report
7. AUTHOR(s) S.B. Segall, H.R. Hiddleston, H. Takeda, S. VonLaven, R. Holsinger, J. Ward, J. Richardson W. B. Colson		6. PERFORMING ORG. REPORT NUMBER
9. PERFORMING ORGANIZATION NAME AND ADDRESS KMS Fusion, Inc. 2621 South State Rd., P.O. Box 1567 Ann Arbor, Michigan 48106		8. CONTRACT OR GRANT NUMBER(s) N 00014-80-C-0614
11. CONTROLLING OFFICE NAME AND ADDRESS Defense Contract Administration Services Management Area, Detroit McNamara Federal Bldg, 477 Michigan Avenue Detroit, Michigan 48226		10. PROGRAM ELEMENT, PROJECT, TASK AREA & WORK UNIT NUMBERS
14. MONITORING AGENCY NAME & ADDRESS (if different from Controlling Office) Office of Naval Research 1030 Green Street Pasadena, CA 91106		12. REPORT DATE January 21, 1983
		13. NUMBER OF PAGES 63
		15. SECURITY CLASS. (of this report) Unclassified
		15a. DECLASSIFICATION/DOWNGRADING SCHEDULE
16. DISTRIBUTION STATEMENT (of this Report) Unlimited		
17. DISTRIBUTION STATEMENT (of the abstract entered in Block 20, if different from Report)		
18. SUPPLEMENTARY NOTES		
19. KEY WORDS (Continue on reverse side if necessary and identify by block number) Free Electron Laser, wiggler magnet, electrostatic accelerator, wave propagation in cylindrical coordinates, two-stage FEL, FEL computer simulation, resonant cavities		
20. ABSTRACT (Continue on reverse side if necessary and identify by block number) This paper reviews continuing work in support of a two-stage free electron laser (FEL) experiment to be performed at the University of California, Santa Barbara. The quasioptical resonant cavity structure that will be used in this experiment is described and scaling of second stage output with a number of system parameters is given. Absorption, diffraction, and mode conversion losses are calculated for the long wavelength pump field for a simple unoptimized cavity design, and an experimental facility to measure		

losses in a test cavity is described, a design concept for a permanent magnet helical wiggler to be used in this experiment is presented. Deficiencies of the present accelerator are described and corrective measures are suggested. A conceptual design for an accelerator that could be used with a high power, two-stage FEL is presented. The three-dimensional wave equation for an FEL with either a magnetic or electromagnetic pump field is derived and an incremental solution in cylindrical coordinates is developed. A resonant particle model is used to obtain information on phase shift and gain in two-dimensional cylindrically symmetric systems.

REVIEW OF TWO-STAGE FEL RESEARCH AT KMS FUSION

(January through September 1982)

by

S. B. Segall
 H. R. Hiddleston
 H. Takeda
 S. Von Laven
 R. Holsinger*
 J. Ward*
 J. Richardson*
 W. B. Colson*

KMS Fusion, Inc.
 P.O. Box 1567
 Ann Arbor, MI 48106

January 21, 1983

Accession For		
NTIS GRA&I	<input checked="" type="checkbox"/>	
DTIC TAB	<input type="checkbox"/>	
Unannounced	<input type="checkbox"/>	
Justification		
By		
Distribution/		
Availability Codes		
Dist	Avail and/or	Special
A		



*Consultants

83 05 26 .03 9

Table of Contents

	<u>Page</u>
A. Introduction and Summary	1
B. Two-Stage FEL Scaling	4
C. Resonant Cavity Design	13
1. Absorption Losses	13
2. Mirror Diffraction Losses	16
3. Mode Conversion Losses	17
D. Measurement of Cavity Q	21
E. Permanent Magnet Helical Wiggler Design	23
1. Multipole Rings	23
2. Helical Wiggler	26
3. Dipole Ring Tuning	31
F. Accelerator Studies	33
1. Deficiencies of the Present UCSB Accelerator	33
2. Control of Voltage Droop	36
3. Control of Voltage Ripple	38
4. Accelerator Power System Limitations	39
5. Design of An Accelerator for a High Power FEL	39
G. Multidimensional FEL Simulation Code	43
1. The Three Dimensional Wave Equation	45
2. Incremental Solution of the Wave Equation	51
3. Solution of the Wave Equation in Cylindrical Coordinates	53
4. Resonant Particle Dynamics in Two-Dimensions	55
H. References	61
I. Distribution List	62

A. Introduction and Summary

KMS Fusion, Inc. began investigating the two-stage free electron laser (FEL) concept in June of 1980. Since then we have developed computer simulation codes to model the interactions taking place between the electron beam and the magnetic and electromagnetic fields in the two-stage FEL and have identified parameter regimes in which such a device is likely to operate successfully. The work reported here is in support of a two-stage FEL experiment that will be performed at the University of California Santa Barbara (UCSB) in collaboration with Luis Elias and the FEL group at UCSB using their electrostatic accelerator.

In a two-stage free electron laser a low energy (\sim few MeV) electron beam is used to produce short wavelength (~ 100 - $1000 \mu\text{m}$) radiation. This is done in two steps. First, the electron beam is passed through a wiggler magnet to produce long wavelength (~ 100 - $1000 \mu\text{m}$) radiation. This radiation is then backscattered from the electron beam to produce the short wavelength radiation. Useful amounts of short wavelength radiation can only be produced if the long wavelength electromagnetic field is very intense ($\sim 10^8 \text{ W/cm}^2$).

During the past year we have developed a resonant cavity design for containing the electromagnetic pump field radiation, which provides a long, narrow, high-intensity region for the FEL interaction to take place while expanding the beam rapidly outside the interaction region to minimize the overall cavity length needed to protect the end mirrors. This quasioptical cavity design is shown in Figure 1.

The design has a number of unique features. A low loss TE_{01} mode is preferentially propagated in the cylindrical waveguide. This mode has an annular intensity distribution with intensity minima at the walls and on axis. Holes in the centers of the cavity end mirrors permit the second-stage short-wavelength radiation to leave the cavity with negligible pump field losses in the preferred TE_{01} mode.

Because the TE_{01} mode has only azimuthal wall currents, it can propagate in a segmented waveguide structure. Segmenting the waveguide prevents all modes except TE_{0N} modes from propagating in the waveguide and also permits introduction of an axial electric field to optimize gain in both the first and second stages of the FEL.

TWO-STAGE FEL EMPLOYING AN OVERMODED CYLINDRICAL WAVEGUIDE

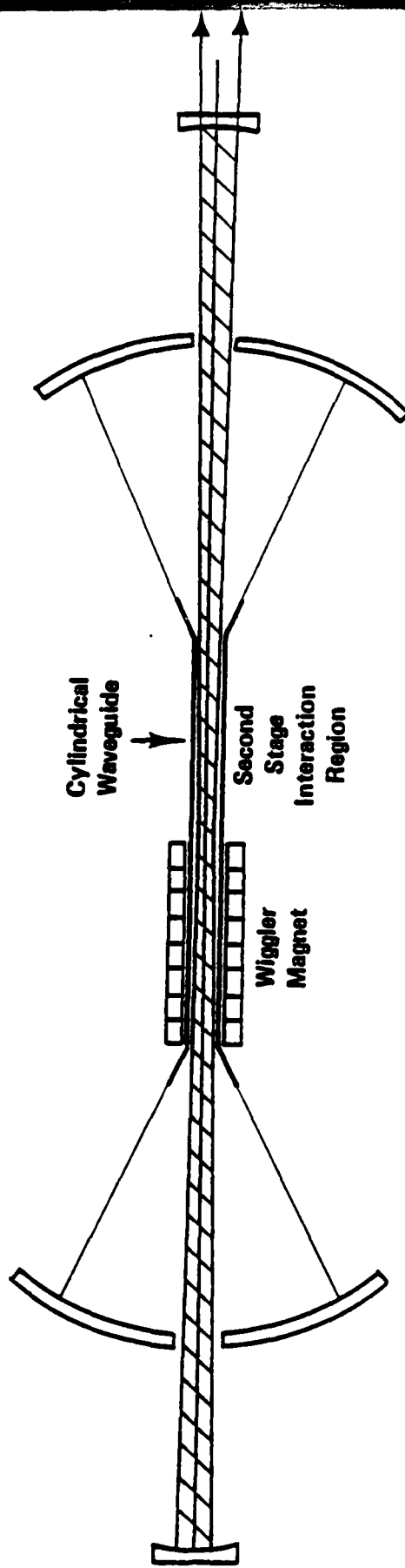


Figure 1

The polarization of the TE_{01} mode is linear but varies as a function of axial position. A helical wiggler magnet is, therefore, needed to fully excite the TE_{01} pump field mode. For best coupling to the pump field mode it is also desirable to use an annular electron beam.

During the period January - September, 1982 we have investigated this quasioptical cavity design in more detail and have begun the process of hardware design. We have also started developing facilities to test this hardware and characterize it before it is used in an FEL experiment. In addition, we have investigated problems associated with electrostatic accelerators used to drive a two-stage FEL and have identified accelerator concepts that could be scaled to high average currents and high laser power.

In this report we summarize the work that has been completed over the past nine-month period. In Section B, laser output power is calculated for the second stage of a two-stage FEL over the range of parameters expected in the experiment to be conducted at UCSB. For output powers up to 1 kW, second stage output power was found to increase as the cube of the pump field intensity for constant electron current, and as the sixth power of the electron current when the pump field intensity is assumed to increase linearly with electron current.

In Section C, absorption, diffraction, and mode conversion losses for the long wavelength pump field radiation are calculated for a simple quasioptical cavity configuration. Absorption losses were found to be about 0.5% per round trip and mode conversion losses about 1.6%. Diffraction losses could be made less than 0.2%. The cavity considered consisted of a cylindrical pipe and two mirrors. We believe that with properly designed horns at the ends of the waveguide to optimally match the waveguide to free space modes, mode conversion losses could be greatly reduced. Reduction of absorption losses by cooling the cavity structure could be considered if mode conversion and diffraction losses can be made small compared with absorption losses. To measure cavity losses experimentally before incorporating the cavity into an FEL experiment, we are setting up a microwave cold test facility. This facility is described in Section D.

For high efficiency, continuous FEL operation, the wiggler magnet used in the first stage of the two-stage FEL would have to be either superconducting

or made of permanent magnets. Linear wigglers are commonly made using permanent magnets, but helical wiggler magnets employing permanent magnets have not yet been built. We are, therefore, investigating the design of a permanent magnet helical wiggler structure. Such a structure could be assembled using an array of permanent magnet dipole rings. In Section E, we describe such a device, determine the fields that could be produced using SmCo_5 permanent magnets, and indicate a process that could be used to tune such a wiggler to correct for field nonuniformities.

In order to perform a successful two-stage FEL experiment, several deficiencies of the present UCSB accelerator must be corrected. These include excessive droop and ripple in the accelerator voltage, an inadequate power system, and the ability to accept only a very small ($\sim 1\%$) energy spread. In Section F, we indicate steps that could be taken to correct these deficiencies so that a proof of principle two-stage experiment could be carried out at the UCSB facility. We also present a design concept for a second generation electrostatic accelerator that could be used to operate a high-power two-stage FEL.

To improve our capability to model FEL systems in general and the two-stage FEL experiment in particular, we have developed a technique for modeling the propagation of laser radiation in a free electron laser in two and three dimensions. In Section G of this report, we derive a three-dimensional wave equation for the electromagnetic wave in an FEL using a basis vector formalism. We then show how this wave equation can be solved using Fourier transforms in Cartesian coordinates. The technique is extended to cylindrical coordinates, but problems arise because fast Fourier transform techniques cannot be used to obtain an incremental solution to the radial part of the wave equation. An approximation that permits the use of the fast Fourier transforms is introduced and a method is developed to insure the accuracy of the solution over a finite spatial mesh. A simplified two-dimensional model of the interaction of the electron beam with an axisymmetric radiation field profile is used to obtain information on the effect of radial variation of the laser field on trapping.

B. Two-Stage FEL Scaling

Basic scaling relationships for a two-stage FEL have been obtained using a simple one-dimensional resonant particle amplifier simulation code. The experimental variables that were found to have the greatest effect on second

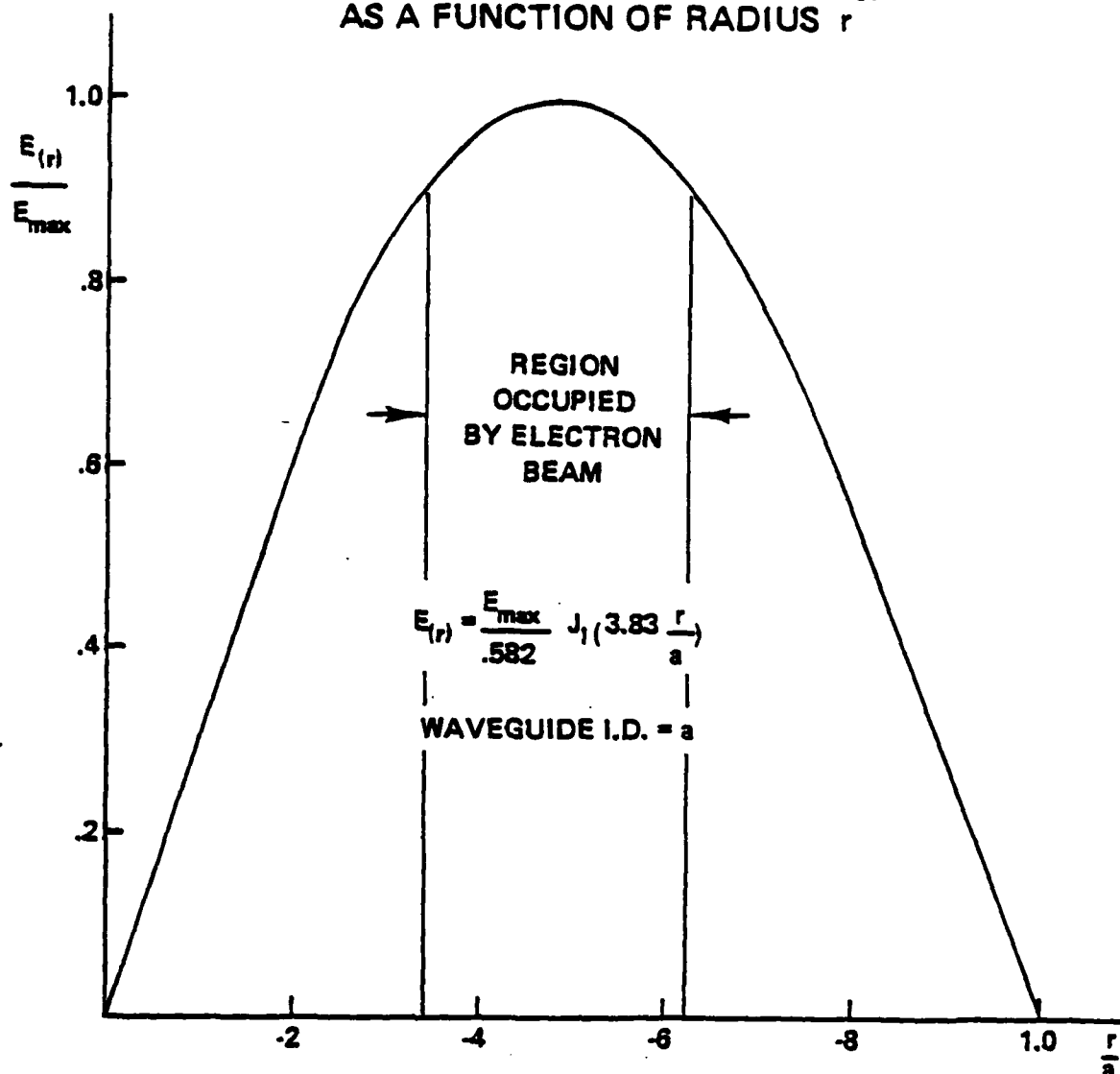
stage output power are the intensity of the electromagnetic(em) pump field produced in the first stage, the electron beam current, and second-stage optical system losses. We have calculated laser gain over a range of values for the pump field intensity, laser field intensity, and electron current assuming the resonant cavity structure of Figure 1 and using accelerator and resonant cavity parameters that are expected for the UCSB two-stage FEL experiment.

In our calculations we assume the electron energy is 3 MeV, the fractional electron energy spread is 10^{-4} , and electron current is in the range between 2 and 20 amp. The length of the second stage interaction region is assumed to be 3 m and the pump field wavelength is assumed to be 1 mm, which gives a laser wavelength of 5.3 μm . The diameter of the cylindrical waveguide is assumed to be 2.44 cm.

An annular electron beam is assumed to interact with the region of peak intensity of the em pump field (see Figure 2). The cross sectional area of the interaction region is assumed to be 1.26 cm^2 . In Figure 3, second stage output power, P_{out} , is plotted as a function of laser power at the input end of the second stage interaction region, P_{Lin} , for a number of values of the pump field power. P_{out} is obtained assuming all of the laser light produced in the amplifier is available as output power. This is probably a reasonably good assumption if several percent of the light is removed from the cavity on every pass. If total cavity losses must be kept below a percent, then a significant fraction of the light produced may not be available as useful output power.

In Figure 3 we see that laser output power increases both with increasing pump field intensity and increasing input laser intensity. In an FEL oscillator at its equilibrium operating point, at which optical system losses just equal laser gain, the input laser power and pump field power will not be independent quantities. Superimposed on Figure 3 are two curves for 1% and 10% amplification. If, the optical system is designed to produce 10% loss per pass, only the region of parameter space above the 10% gain curve will be accessible. This places a lower limit on the pump field power needed to obtain a given laser output power. For example, with the parameters used in Figure 3, if the pump field power is 10^8 watts and optical system losses are 10% per pass, the maximum output power that could be attained would be 0.45 watt.

ELECTRIC FIELD AMPLITUDE FOR TE_{01} MODE AS A FUNCTION OF RADIUS r



$E(r)$ is within 10% of E_{\max} in interval $.34 \leq r/a \leq .62$

Bucket height (proportional to $E(r)^{1/2}$) varies by 5% over same interval

Cross sectional area of electron beam = .27 of waveguide cross section

$\langle E(r) \rangle = .96 E_{\max}$ in interaction region. E_{\max} occurs at $r/a = .47$

Example: $a = 1.22$ cm, guide area = 4.68 cm^2

electron beam area = 1.26 cm^2

Figure 2

OUTPUT POWER SCALING FROM EM PUMP FEL (UCSB PARAMETERS)

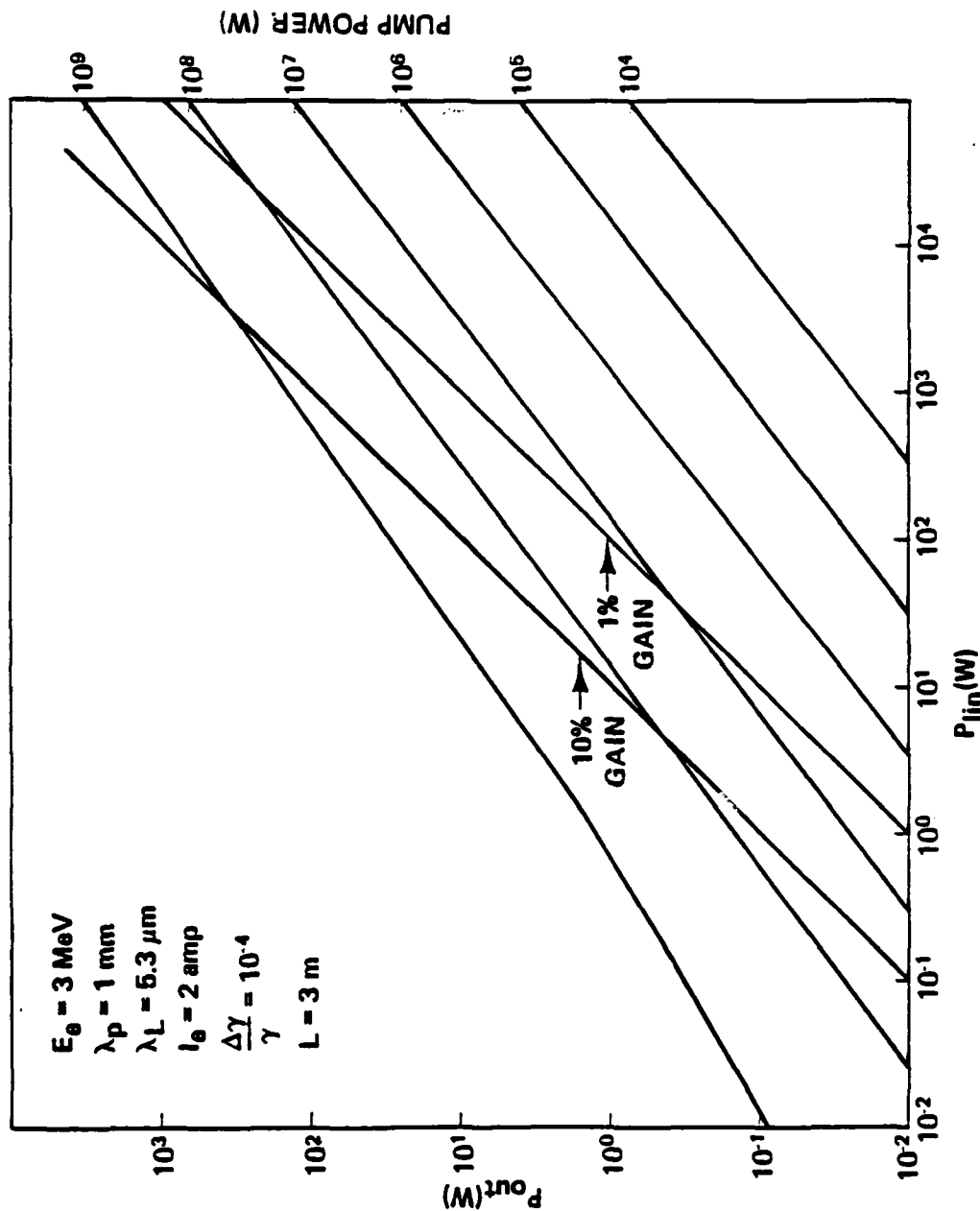


Figure 3

In Figure 4 output power is plotted as a function of pump field power for the parameters of Figure 3. Two curves are shown, one for 10% loss per pass in the second-stage optical system, the other for 1% loss. The slopes of these curves indicate that laser output power scales as the cube of the pump field power. We also see that with a two-amp beam very intense pump fields are needed to obtain even modest laser output powers.

Pump field power is determined by dividing the power gain of the pump field by the fraction of the energy lost per cavity round trip. Input power to the pump field is limited by generator capacity in the accelerator and the maximum energy with which an electron can lose and still return to the dome of the accelerator.

The generator in the accelerator at the present time provides 20 kw of power in the dome. This is sufficient to provide for an average of 10 keV energy loss per electron for a 2-amp beam if all of the power can be used for this purpose. Electron gun voltage is 50 kV so that losses of up to a few tens of keV for some electrons, with an average 10 keV / electron loss for the entire beam, is acceptable for collection of the return beam.

Round trip cavity losses are initially expected to be between 1 and .1% for the pump field radiation. Losses may be reduced below .1% at a later time with improvements in cavity design. With 20 kw of input power and cavity losses of .1% per pass, the intracavity power would be 2×10^7 watts. In order to obtain pump field powers of 10^8 watts or greater, more generator power must be provided for the electron beam, a greater energy loss per electron must be permitted, and cavity losses must be reduced. It is expected that all of these things will happen as operating experience is gained and the system is upgraded.

It is presently planned to modify the UCSB accelerator to increase the maximum beam current from 2 to 20 amp. It is, therefore, important to know how laser output is expected to scale with increasing beam current. Several parameters will change as a result of increasing the beam current.

Increasing the electron beam current will increase the gain in the first stage of the laser as well as in the second stage. Therefore, the pump field intensity will be greater than could be achieved with a lower beam current. If the fraction of the electron energy converted to long wavelength radiation remains the same, the pump field power will increase

OUTPUT POWER SCALING AS A FUNCTION OF PUMP FIELD POWER (CONSTANT CURRENT)

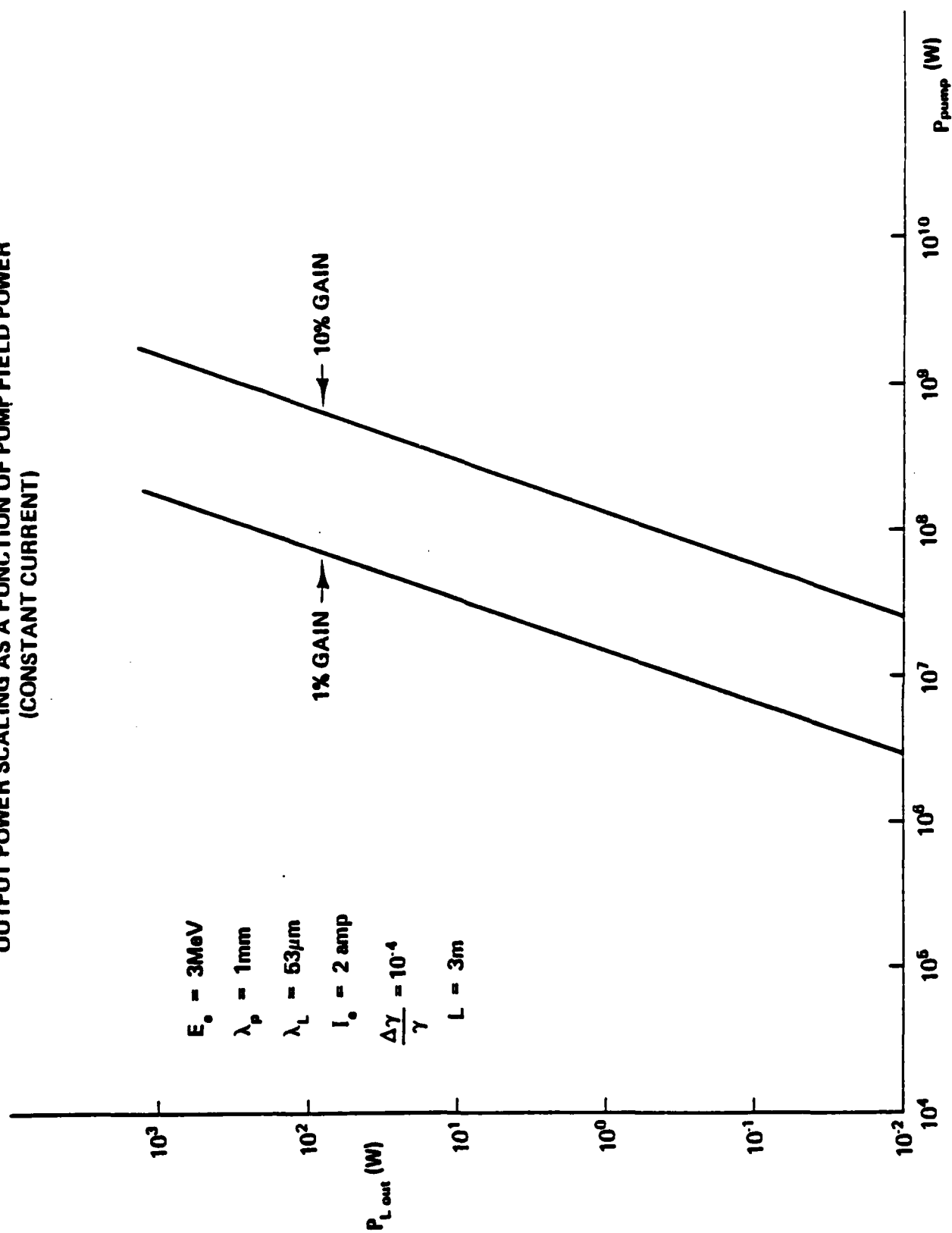


Figure 4

linearly with electron current. It may be possible to increase the pump field power more rapidly than linearly, however, since conversion efficiency could increase at the higher pump field intensity.

For the pump field power to increase, the power supplied by the generator must also increase. This might be done by increasing the generator capacity, storing generated power between pulses, or a combination of the two. In determining the scaling of second-stage output power with beam current, we will make the conservative assumption that the pump field power increases only linearly with electron current due to accelerator system limitations. Accelerator limitations will be less of a factor for second stage gain in the UCSB experiment, provided conversion efficiency in the second stage is small compared to the first stage.

The second-stage output power will increase much more rapidly than linearly with increasing beam current, because both the pump field intensity and the second stage gain at a given pump field intensity will increase. If the optical system has a fixed percentage loss per pass, the equilibrium operating point will shift upward as the curve of P_{out} as a function of P_{Lin} rises relative to a line of constant gain (see Figure 3).

The effects of increased pump intensity, increased second stage gain at a given pump field intensity, and shift of the equilibrium operating point are all included in the curves of laser output power as a function of electron current plotted in Figure 5. Curves are shown for optical systems with both 10% and 1% losses per pass. For peak output powers below several kilowatts, P_{out} scales approximately as the sixth power of the electron current. Above 10 kW output power increases more slowly with increasing current. The reason for the difference in scaling is that at the lower laser powers the fraction of the electron distribution contributing to laser gain increases as the intracavity laser intensity increases. Above a certain power level the phase space buckets are large enough to trap most of the electrons in the beam, so that the fraction trapped remains constant.

The output power shown in Figure 5 is the peak power that could be obtained in the UCSB experiment for the assumed resonant cavity losses.

SCALING OF OUTPUT POWER WITH ELECTRON CURRENT FOR UCSB TWO-STAGE FEL

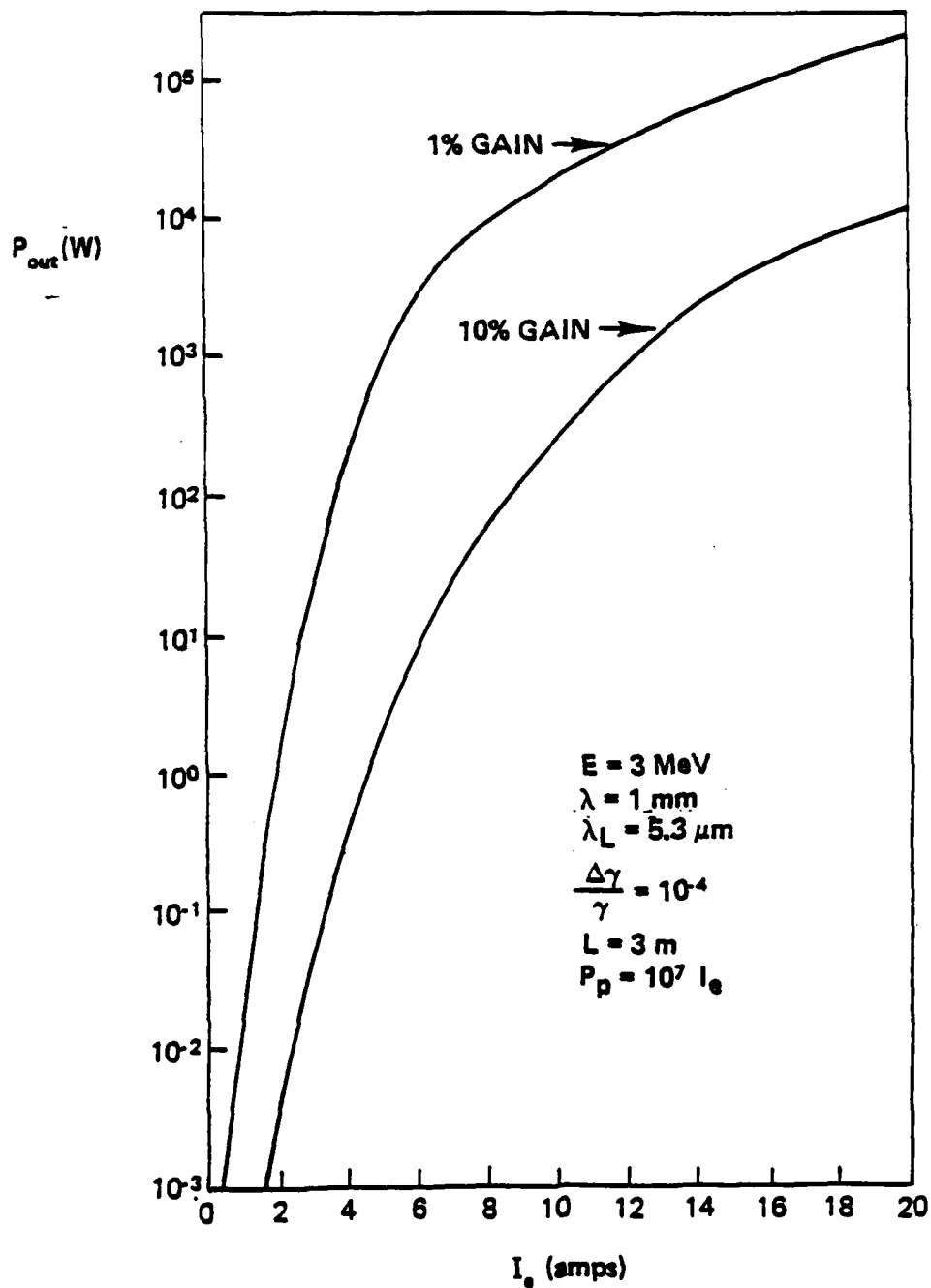


Figure 5

Since the accelerator will lose charge at a more rapid rate than it can be replenished by the input current, the accelerator will operate in a pulsed mode. During each electron pulse, both the pump field and the laser field must build up from spontaneous emission.

If the time needed to reach equilibrium is longer than the electron pulse, the peak laser output power will be less than the equilibrium value. Electron pulse length is directly dependent on the efficiency with which the electron beam is returned to the dome of the accelerator. If 1% of the electron beam is lost in the beam transport system the electron pulse length would be about 80 μ sec for a 2-amp beam in the UCSB accelerator and about 8 μ sec for a 20-amp beam. Initial experiments have produced collection efficiencies of about 96% without an FEL amplifier in the beam line. Collection of 99% or better with the FEL in operation are a long range goal. We have assumed an annular electron beam in the calculation. The first experiments will not be done with an annular beam, and therefore only part of the electron beam will interact with the high intensity pump field, lowering the effective electron current.

In conclusion, we have found that laser output power should vary as the sixth power of the electron current in the UCSB two stage FEL experiment. If the electron current is held constant, laser output power will vary as the third power of the pump field intensity. Decreasing optical system losses increases the amount of laser light produced in the cavity. Optical system losses include both the output power and dissipative losses such as mirror absorption and scattering. Dissipative losses in the second stage can probably be kept to a percent or less per round trip optical pass.

The scaling with pump field power and electron current for the two-stage FEL indicates that prospects for developing a high-power high-efficiency device based on this concept appear very good. If the UCSB experiment works as predicted, high average power devices could be built with electron currents not exceeding 20 amp. This would require developing an accelerator system with sufficiently low losses and sufficiently high input current to operate in a D.C. mode. It would also require much higher power conversion from the electron beam to the

optical beam and higher pump field power levels. As will be discussed in the following sections, this scaleup may be accomplished with existing state of the art technology.

C. Resonant Cavity Design

The pump field cavity must be designed to minimize cavity losses. Cavity losses reduce the maximum pump field intensity that can be attained in the interaction region and also reduce the overall efficiency of the device. There are three main classes of losses that can occur in the cavity - absorption losses, diffraction losses and mode conversion losses.

1. Absorption Losses: For good conductors, the surface resistance R_s can be written as¹

$$R_s = \frac{1}{\sigma \delta} \quad (C-1)$$

where σ is the conductivity and δ is the skin depth. The skin depth is given by

$$\delta = (\pi \sigma \mu_0 f)^{-1/2} \quad (C-2)$$

where f is the frequency of the wave. For normal incidence illumination it can be shown theoretically^{2,3} and experimentally⁴ that the absorption loss is given by

$$P_r = P_i (1 - 4 R_s / Z_0) \quad (C-3)$$

where $Z_0 = \mu_0 / \epsilon_0 = 377 \Omega$ is the free space impedance, P_r is the reflected power, and P_i is the incident power.

Table 1 gives conductivity, skin depth, surface resistance, and the dimensionless quantity R_s / Z_0 for a number of different metals at a wavelength of 1 mm. The values in Table I are based on the assumption of idealized surface conditions. Surface contamination and imperfections on grain boundaries could increase absorption by up to a factor of 2.

For the case of a cavity with two copper mirrors at room temperature the round trip cavity transmission factor T_m is given by

$$T_m = 1 - 8 R_s / Z_0 = 0.997 \quad (C-4)$$

Table I

NORMAL INCIDENCE ABSORPTION LOSSES ON THE SURFACE
OF GOOD CONDUCTORS AT ROOM TEMPERATURE $(\lambda = 1 \text{ mm})$

<u>Conductor</u>	<u>Conductivity</u> σ (mho/m)	<u>Skin depth</u> δ (m)	<u>Surface</u> <u>Resistance</u> R_s (Ω)	<u>Loss</u> <u>Factor</u> R_s/z_0
Aluminum	3.54×10^7	1.54×10^{-7}	0.18	4.9×10^{-4}
Copper	5.8×10^7	1.21×10^{-7}	0.14	3.79×10^{-4}
Silver	6.15×10^7	1.17×10^{-7}	0.139	3.68×10^{-4}
Gold	4.5×10^8	1.37×10^{-7}	0.16	4.3×10^{-4}

In a cylindrical waveguide the attenuation of the power in a propagating wave is given by

$$P(z) = P_i e^{-\alpha z} \quad (C-5)$$

For a TE_{01} wave the attenuation coefficient, α , is given by^{2,5}

$$\alpha = \frac{2R_s}{aZ_0} \frac{(f_c/f)^2}{\sqrt{1 - (f_c/f)^2}} \quad (C-6)$$

where a is the waveguide radius, f is the frequency of the radiation, and f_c is the waveguide cutoff frequency. For a TE_{01} mode

$$\frac{f_c}{f} = \frac{u}{2\pi a} \lambda \quad (C-7)$$

where u is the value of the first off-axis zero of the J_1 Bessel function. $J_1(u) = 0$ for $u = 3.83$. For $\lambda = .1$ cm and $a = 1.22$ cm, $f_c/f = 0.05$ and $\alpha = 1.55 \times 10^{-4} \text{ m}^{-1}$. For a 5-m-long copper waveguide, at room temperature, the round trip transmission factor T_g will be given by

$$\begin{aligned} T_g &= e^{-2\alpha L} \\ &= .998 \end{aligned} \quad (C-8)$$

Total transmission losses due to absorption in both the mirrors and the waveguide in one cavity round trip will therefore be

$$\text{Absorption loss} = 1 - T_m T_g = 1 - .995 = 5 \times 10^{-3} \quad (C-9)$$

Whether a loss rate this high would be tolerable in a high power two-stage FEL depends on the fraction of the electron energy converted to usable photon energy per pass, the overall laser efficiency required, and the size of the losses compared with other system losses. Absorption losses could be made almost arbitrarily low, if required, by cooling the metallic surfaces of the cavity. Cooling should only be considered after it is demonstrated that absorption losses are the dominant cavity loss mechanism.

2. Mirror Diffraction Losses: If the radius of a free space mode leaving the waveguide is ω_0 , then the radius of that mode at any distance z from the waveguide is given by

$$\omega(z) = \omega_0 \left(1 + \left(\frac{z}{z_0} \right)^2 \right)^{1/2} \quad (C-10)$$

where

$$z_0 = \frac{\pi \omega_0^2}{\lambda} \quad (C-11)$$

If we assume the intensity pattern is primarily that of a TEM_{01}^* annular mode, the intensity across the beam is given by

$$I(r) = I(0) e^{-\rho} \quad (C-12)$$

where

$$\rho = \frac{2r^2}{\omega^2} \quad (C-13)$$

The value chosen for ω_0 is some fraction α of the waveguide radius, a , which gives a good match between the free space and waveguide cavity modes.

$$\omega_0 = \alpha a \quad (C-14)$$

If we assume that the TE_{01} waveguide mode is converted into a TEM_{01}^* free space mode then a best fit value for α is $\alpha = 0.5$. For $a = 1.22$ cm, $\lambda = 0.1$ cm, and an assumed distance of 2 m between the end of the waveguide and the mirror, the beam radius at the mirror, ω_m , will be 10.45 cm.

Now

$$\int \rho e^{-\rho} d\rho = -(1+\rho) e^{-\rho}, \quad (C-15)$$

and the value of this integral from 0 to ∞ equals 1. Therefore to find the fraction of the cavity radiation inside a mirror of radius A we only have to evaluate (C-15) from 0 to $\rho(A)$. For example, if we chose $A = 2\omega_m$ then $\rho(A) = 8$ and .997 of the radiation will hit the mirror. If $A = 2.5 \omega_m$ then .99995 of the radiation leaving the waveguide will intercept the mirror. Therefore, diffraction losses around the outside

of the mirror can be made arbitrarily small by making the mirror sufficiently large.

The short wavelength radiation will also come out of the waveguide as an annular beam, but it will spread much less. For $5.3 \mu\text{m}$ radiation the beam radius at a mirror 2 m from the waveguide would be 0.61 cm, essentially the same as at the waveguide. If we make a hole in the mirror with a radius 2.5 times larger, virtually no short wavelength radiation will hit the mirror. From (C-15) the fraction of the long wavelength radiation that would be lost through this hole would be 1×10^{-3} with a round trip loss due to diffraction of 2×10^{-3} . This loss could be reduced by placing the mirrors farther from the waveguide.

3. Mode Conversion Losses: During the period covered by this report a model has been developed to calculate losses from the simplest possible quasioptical cavity consisting of a pipe and two mirrors. In this model a TE_{01} waveguide mode is converted to a linear combination of TEM_{p1}^* modes at the end of the waveguide. The individual free space modes propagate to the mirror and back. The returning power feeds the TE_{01} mode as well as other waveguide modes and is partially lost around the outside of the waveguide. Losses are assumed to consist of all energy not reconverted into the TE_{01} mode.

The discontinuity at the end of the waveguide results in reflection of part of the field back into the waveguide. For a simple pipe the reflection coefficient R_g is given by

$$R_g = (Z_0 - Z_g) / (Z_0 + Z_g) \quad (\text{C-16})$$

where

$$Z_g/Z_0 = (1 - (f_c/f)^2)^{1/2} \quad (\text{C-17})$$

For the case we are considering $R_g = 6.25 \times 10^{-4}$. This reflection need not degrade cavity performance if the reflected wave is in phase with the wave reflected from the cavity end mirror. We will assume this to be the case. Improved cavity designs with conical horns at the end of the waveguide could significantly reduce this reflection.

Inside the waveguide the electric field has the form

$$E_{\theta}(r, z, t) = E_{\theta}(r) \cos(kz - \omega t) \quad (C-18)$$

where $E_{\theta}(r)$ is proportional to the J_1 Bessel function, $J_1(3.832 r/a)$.

At the end of the waveguide the Bessel function mode is reexpressed as a linear combination of Gauss LaGuerre modes with the azimuthal component of the electric field given by

$$E_{\theta p}(u) = \sqrt{\frac{2u}{\pi \omega_0^2}} L_p^{(1)}(u) \frac{1}{\sqrt{p+1}} e^{-u/2} \quad (C-19)$$

where

$$u = \frac{2r^2}{\alpha^2 a^2} \quad (C-20)$$

and

$$\alpha = \omega_0/a \quad (C-21)$$

ω_0 is the beam-waist radius of the free space beam at the end of the guide. The associated LaGuerre polynomials are obtained from the relation

$$L_p^{(1)}(u) = -\frac{d}{du} L_{p+1}(u) \quad (C-22)$$

The waveguide and free space modes are normalized so that

$$\int_0^a 2\pi r dr E_{\theta}^2(r) = 1 \quad (C-23)$$

and

$$\int_0^{\infty} 2\pi r dr E_{\theta p}^2 = 1 \quad (C-24)$$

At the boundary the waveguide mode can be expressed in terms of the free space modes in the following way:

$$E_{\theta} = \sum_{p=0}^{\infty} C_p E_{\theta p} \quad (C-25)$$

where

$$C_p = \int_0^a 2\pi r dr E_{\theta}(r) E_{\theta p}(2r^2/a^2\alpha^2) \quad (C-26)$$

A computer program has been written to solve these equations. Cases were considered with up to 12 free space modes. A range of values for the parameter α were tried. For 12 modes a best fit was obtained for

$\alpha = 0.3$. The values of the coefficients C_p for this case are given in Table 2. The sum of the squares of the first 12 terms, $\sum_{p=0}^{11} C_p^2$, is also given. The deviation of this sum from unity is a measure of the contribution due to modes with $p > 11$. C_r is the remaining amplitude if only one higher order mode were needed to completely represent the waveguide mode at the boundary.

Table II

Coefficients for Expansion of TE_{01} modes as a series of Gauss Laguerre free space modes for $\alpha = 0.3$

$C_0 = .6153$	$C_6 = -.3733 \times 10^{-1}$
$C_1 = -.5828$	$C_7 = .2040 \times 10^{-1}$
$C_2 = .4400$	$C_8 = .1125 \times 10^{-1}$
$C_3 = -.2695$	$C_9 = -.1388 \times 10^{-1}$
$C_4 = .1139$	$C_{10} = -.5760 \times 10^{-2}$
$C_5 = -.4748 \times 10^{-2}$	$C_{11} = .8875 \times 10^{-2}$
$C_r = .1473 \times 10^{-1}$	$\sum_{p=0}^{11} C_p^2 = .9998$

When the radiation leaving the guide propagates to the mirrors and back to the waveguide, the different modes do not stay in phase. The phase shift of the modes with $p > 0$ relative to the $p=0$ mode is given by

$$\phi_p = 4p \arctan \left(\frac{L_{gm} \lambda}{\pi a^2 \alpha^2} \right) \quad (C-27)$$

where L_{gm} is the distance from the end of the waveguide to the mirror. For $L_{gm} = 200$ cm, $\lambda = .1$ cm, $a = 1.22$ cm and $\alpha = .3$

$$\frac{\phi_p}{4p} = \arctan (47.5) = 88.8 \text{ degrees} \quad (C-28)$$

The modes with small values of p will have relative phase shifts close to zero (multiples of 2π radians) while modes with very large p will have small amplitudes.

The radiation returning to the waveguide is given by

$$\sum_{p=0}^{\infty} C_p E_{\theta p} e^{i\phi_p} = \sum_{j=1}^{\infty} A_j e^{i\phi_j} B_j + \sum_{n=0}^{\infty} q_n E_{\theta n} \quad (C-29)$$

In (C-29) the incoming wave is decomposed into two parts. The first sum on the right hand side are the waveguide modes which may be nonzero for $r < a$ but are equal to zero for $r > a$. The second sum on the RHS of (C-29) represents the remainder of the radiation field outside the waveguide and equals zero for $r < a$.

Multiplying (C-29) by $2\pi r \sum_{p=0}^{\infty} C_p E_{\theta p}$ and integrating using the orthogonality conditions gives

$$\sum_{p=0}^{\infty} C_p^2 e^{i\phi_p} = A_1 e^{i\phi_1} \quad (C-30)$$

This result is obtained because $\sum_{p=0}^{\infty} C_p E_{\theta p}$ is equivalent to the TE_{01} mode in the waveguide ($B_1 = E_{\theta}$), and all the other waveguide modes, B_i ($i > 1$), are orthogonal to it. Outside the waveguide $\sum_{p=0}^{\infty} C_p E_{\theta p} = 0$, so the integrand for the second sum in (C-29) is always zero. The fraction of the returning power converted back into the TE_{01} mode is equal to A_1^2 .

$$\begin{aligned} A_1^2 &= [R_e[A_1 e^{i\phi_1}]]^2 + [I_m(A_1 e^{i\phi_1})]^2 \\ &= \left(\sum_{p=0}^{\infty} C_p^2 \cos \phi_p \right)^2 + \left(\sum_{p=0}^{\infty} C_p^2 \sin \phi_p \right)^2 \end{aligned} \quad (C-32)$$

Taking only the first 12 terms of each sum we get a value for $A_1^2 = 0.9921$. This indicates that practically all of the radiation returning to the waveguide will reenter the guide and again propagate as a TE_{01} mode. Upper and lower bounds on the value that would be obtained if an infinite sum were taken are $\pm A_1^2 \pm 2C_r^2$. The round trip transmission factor for the TE_{01} mode equals A_1^4 since mode conversion would occur at both ends of the waveguide. For the first 12 modes $A_1^4 = .9843 \pm .0008$.

A loss of .8% per round trip pass due to mode conversion is obviously higher than we would like, but this result is only the first cut at modeling an initial unoptimized configuration. Lower losses could be obtained with this same configuration, however, by increasing the distance between the end of the waveguide and the mirrors with a corresponding increase in the size of the mirrors.

D. Measurement of Cavity Q

Modeling calculations of the quasioptical cavity indicate that losses per round trip pass could be kept below 1%. We wish to verify these calculations experimentally before fabricating the hardware to be used in the UCSB two-stage experiment. To do this we are setting up a microwave cold test laboratory in which the Q of cavities similar to that which will be used in the two-stage FEL experiment can be measured. The testing procedures developed in this laboratory will not only provide us with a better understanding of cavity performance, but will also provide us with diagnostic experience that will be needed for the FEL experiment.

We have determined the cold test measurements which will be necessary during the construction and subsequent characterization of the quasi-optical pump cavity. These consist mainly of progressively narrower bandwidth measurements. The test cavity configuration shown in Figure 6 will be used for testing cavity components. The information needed for the design of the pump cavity can be obtained from the test cavity.

The cold testing will be performed at a wavelength of 3 mm. An efficient, reliable mode converter to launch the low loss TE_{01} mode into the circular guide is available at 3 mm, but not at shorter wavelengths. Also, good frequency stability (a few parts in 10^8) is required of the bench source. This stability can be guaranteed at 3 mm, but again not at shorter wavelengths.

Two bench sources will be used to cover the range of bandwidths we need. A frequency-swept backward wave oscillator will provide the wide bandwidth necessary for many of our initial tests and will permit the measurements to be made quickly. These tests include identification of

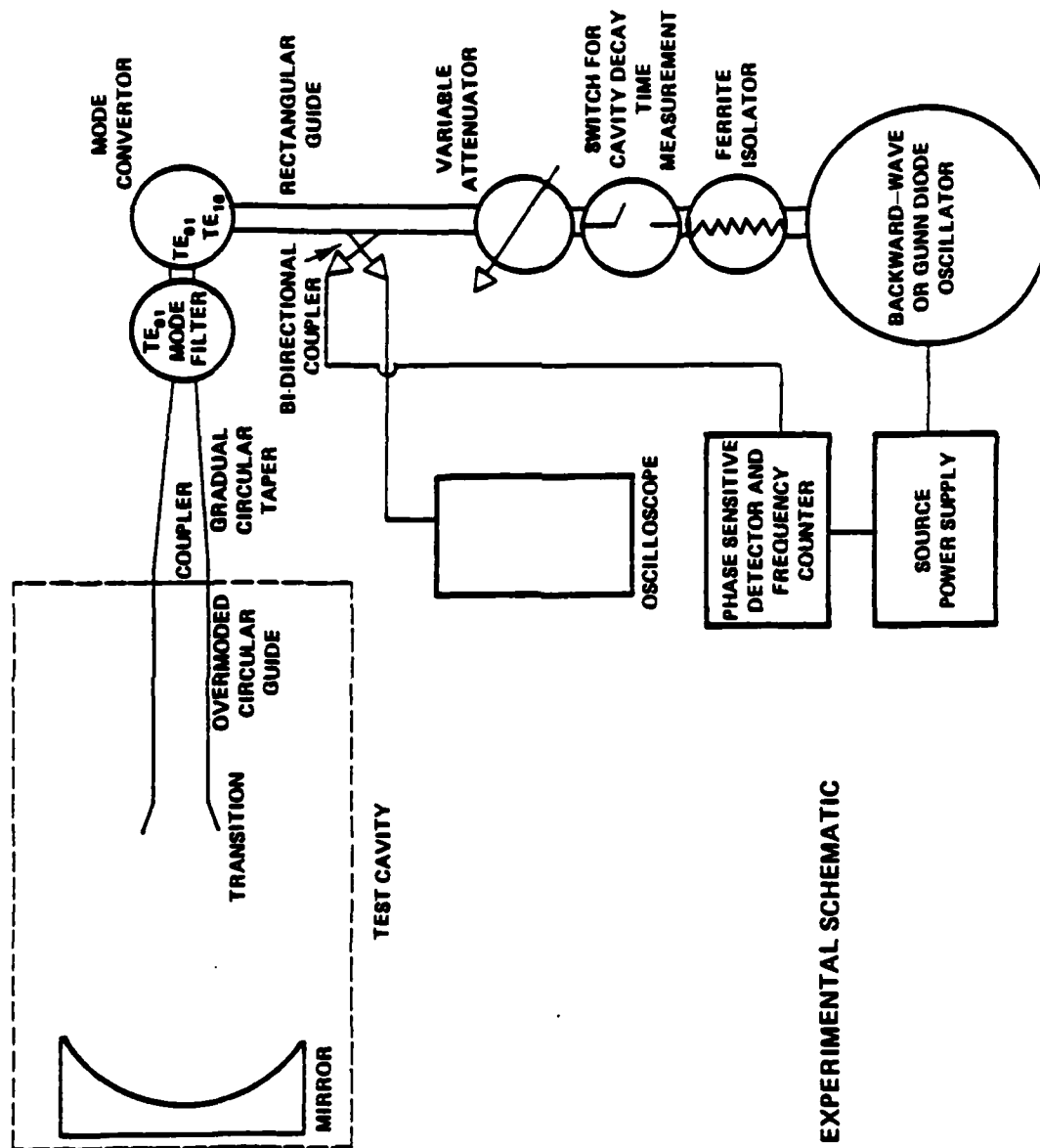


Figure 6

undesired modes and initial Q measurements of the desired mode. Q can be expressed as $f/\Delta f$, where f is the center frequency of the mode, and Δf is its bandwidth, which is proportional to the losses suffered by the mode.

The test cavity is expected to have absorption losses of a few tenths of a percent per round trip pass at room temperature. A comparable amount of power will be transmitted through the element coupling the cavity to the cold test equipment. This coupler will be designed so as not to produce undesired modes. We expect that losses at the waveguide/free-space transition will be less than 0.1% for optimized cavities. The bandwidth corresponding to the total losses will be several parts in 10^7 . Thus, in order to detect improvements in the waveguide/free-space transition, we will need frequency stability of a few parts in 10^8 . A phase locked Gunn diode oscillator meets this requirement and has an adequate power level.

An alternative method of measuring cavity Q is by measuring the 1/e decay time ($\tau_c = Q/2\pi f$) of the natural oscillations of the cavity. This may be done with a high isolation switch (shown in Figure 6) and sensitive diode detector.

E. Permanent Magnet Helical Wiggler Design

A helical wiggler magnet is needed to fully excite the TE_{01} pump field mode. During this contract period we have investigated the possibility of producing this helical wiggler field using an array of permanent magnets. We have found that it is possible to do this and that the magnetic field produced using permanent magnets would have the same form as that which is produced using a bifilar helical winding such as in the Stanford wiggler⁶.

1. Multipole Rings: The building block for a permanent magnet ($SmCo_5$) helical wiggler will be a dipole ring. The design concept for any multipole ring is as follows. If, in a ring of perfect rare earth cobalt (REC) material with inner radius r_1 and outer radius r_2 , the easy axis is continuously rotated according to the relation

$$\alpha = (N+1)\theta, \quad (E-1)$$

then a perfect multipole field of harmonic order N will be produced inside r_1 .⁷ The strength of these multipole fields is, for $N > 2$,

$$|B_N(r_1)| = \left(\frac{N-1}{N}\right) B_r \left[1 - \left(\frac{r_1}{r_2}\right)^{N-1}\right] \quad (E-2)$$

where the harmonic number, N , equals half the number of poles in the magnet ring. For $N = 1$, the dipole field strength is

$$|B_1| = B_r \ln \left(\frac{r_2}{r_1}\right) \quad (E-3)$$

It has been shown⁷ that this multipole ring design produces the strongest possible field for a given amount of REC material. It is not presently possible or practical to produce rings with a continuous easy axis orientation. The solution is to segment the ring into a number of pieces as illustrated in Figure 7. In each segment the easy axis orientation is constant at the value prescribed in (E-1) for a line through the center of the segment.

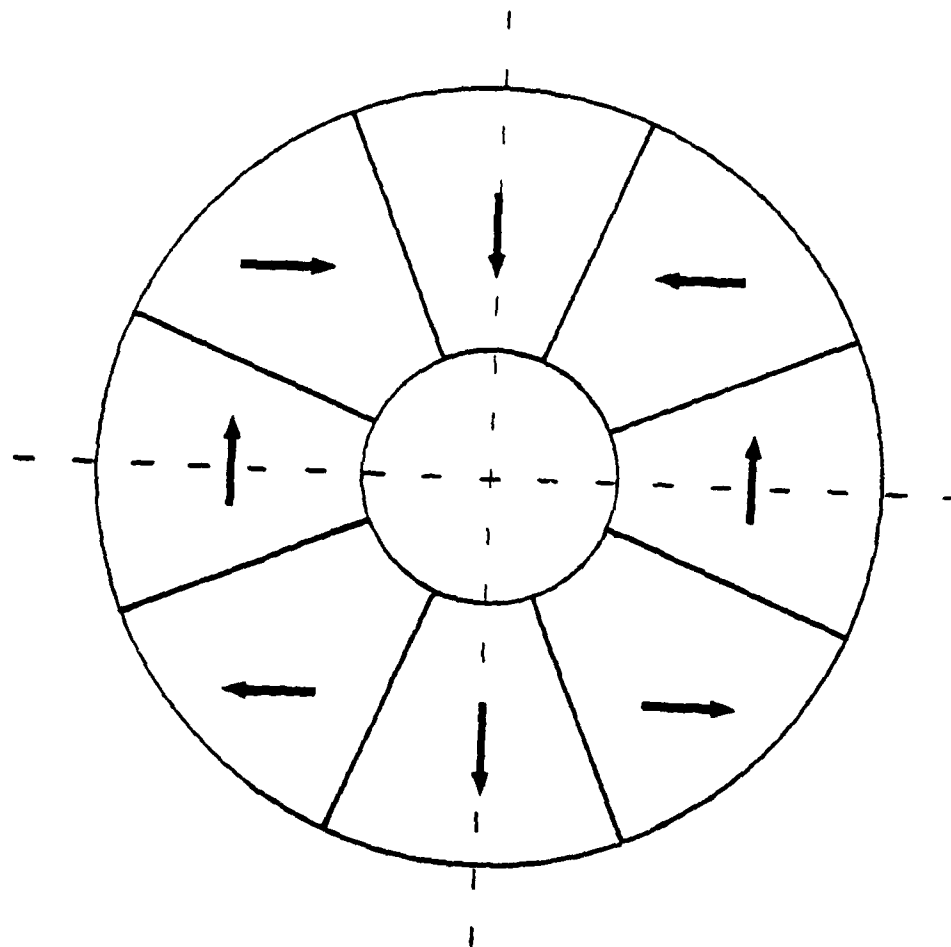
The segmentation of the ring has two consequences. Equations (E-2) and (E-3) are multiplied by form factors, depending on the exact shape of the segments. For trapezoidal segments, the form factor is

$$K_N = \cos^N \frac{\pi}{M} \frac{\sin \frac{N\pi}{M}}{\frac{N\pi}{M}} \quad (E-4)$$

where M is the number of pieces around the ring. For a reasonably large value of M , K_N is close to 1, e.g. for $N = 1$, a dipole magnet, and $M = 8$ pieces, $K_N = 0.90$. The second consequence of segmentation is that the field distribution inside the ring is no longer a perfect multipole, but contains harmonic field errors. The fields in a multipole ring may be expressed as

$$B^*(z) = B_x - iB_y = \sum_n b_n \left(\frac{z}{r_1}\right)^{n-1} \quad (E-5)$$

where the b_n 's are the harmonic multipole field coefficients. It can be shown⁷ that in a perfect segmented multipole ring, only certain terms appear in the series in (E-5):



SEGMENTED RING DIPOLE

Figure 7

$$n = N + vM, \quad v = 0, 1, 2, \dots \quad (E-6)$$

For a dipole with $M = 8$, this series is $n = 1, 9, 17, \dots$ and the first error harmonic is the $n = 9$, 18-pole. The strength of this error depends on the exact geometry of the pieces and the ratio (r_1/r_2) . For 8 trapezoidal pieces in a dipole with $(r_1/r_2) = 1/2$, $|b_9/b_1| = 0.095$. The flux distribution in such a ring is shown in Figure 8.

2. Helical Wiggler: An REC permanent magnet helical wiggler can be constructed by an axial stack of dipole rings where each ring is rotated about the axis relative to its neighbors. For the dipole ring geometry of Figure 7 the expression for the amplitude of the rotating dipole field on axis in such a wiggler is⁸

$$B_h = B_r C_1 \frac{\sin \frac{\pi J}{J}}{\frac{\pi J}{J}} [T(x_1) - T(x_2)] \quad (E-7)$$

with the following definitions:

$$C_1 = \frac{\sin \frac{2\pi}{M}}{\frac{2\pi}{M}}, \text{ the form factor for circular segments,}$$

J = the number of slices per period λ , and

$$T(x) = K_0(x) + \frac{x}{2} K_1(x), \quad x_1 = \frac{2\pi r_1}{\lambda}$$

where K_0 and K_1 are modified Bessel functions of the second kind. The function $T(x)$ is given in Figure 9. Both C_1 and the factor depending on the number of slices per period will be close to 1 for reasonable designs. $T(x_2)$ can be made small for reasonable values of $x_2 = 2\pi r_2/\lambda$. Therefore the dominant term which determines the helical wiggler strength will be the value of $T(x_1)$ corresponding to the ratio r_1/λ . Although (E-7) is strictly correct only for the case of circular segments in the dipole ring, it is a good approximation to the solution with alternate shaped segments such as trapezoids and rectangles, if the proper form factors, K_1 , are substituted for C_1 .

MAGNETIC FIELD OF DIPOLE RING COMPOSED OF 8 TRAPEZOIDAL MAGNET SEGMENTS

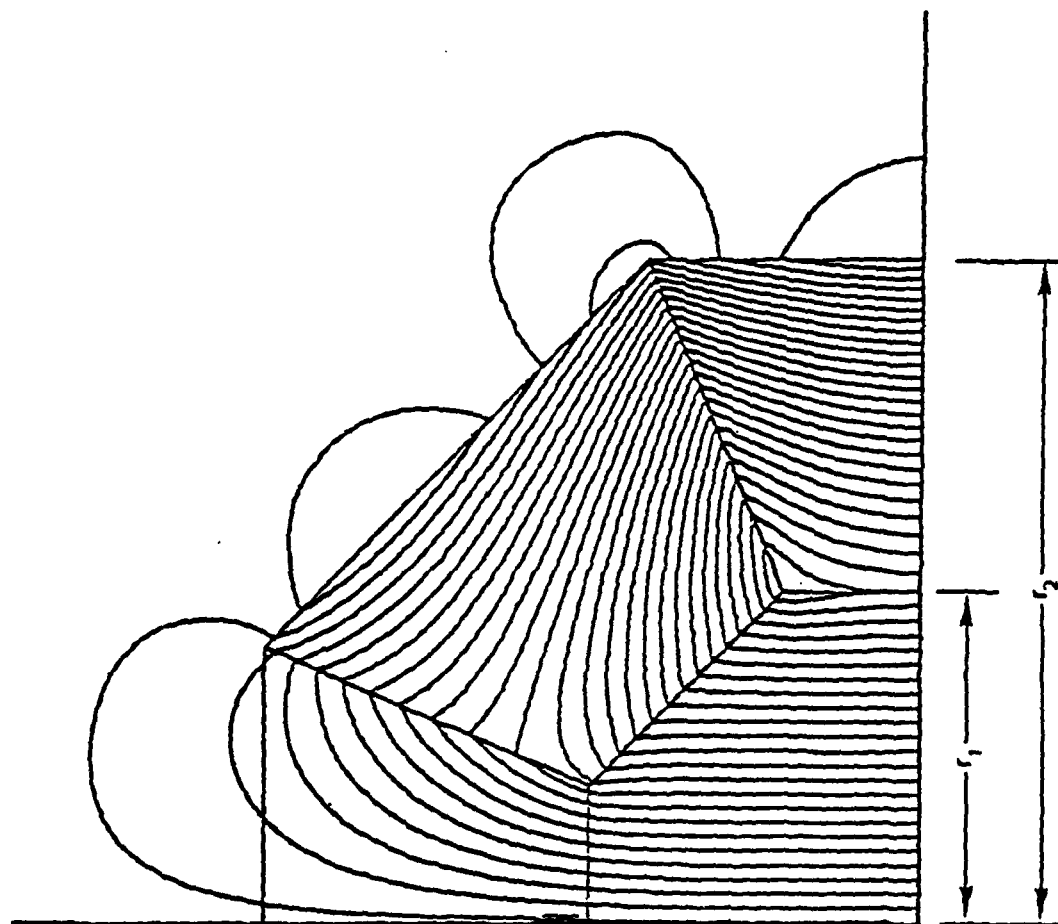


Figure 8

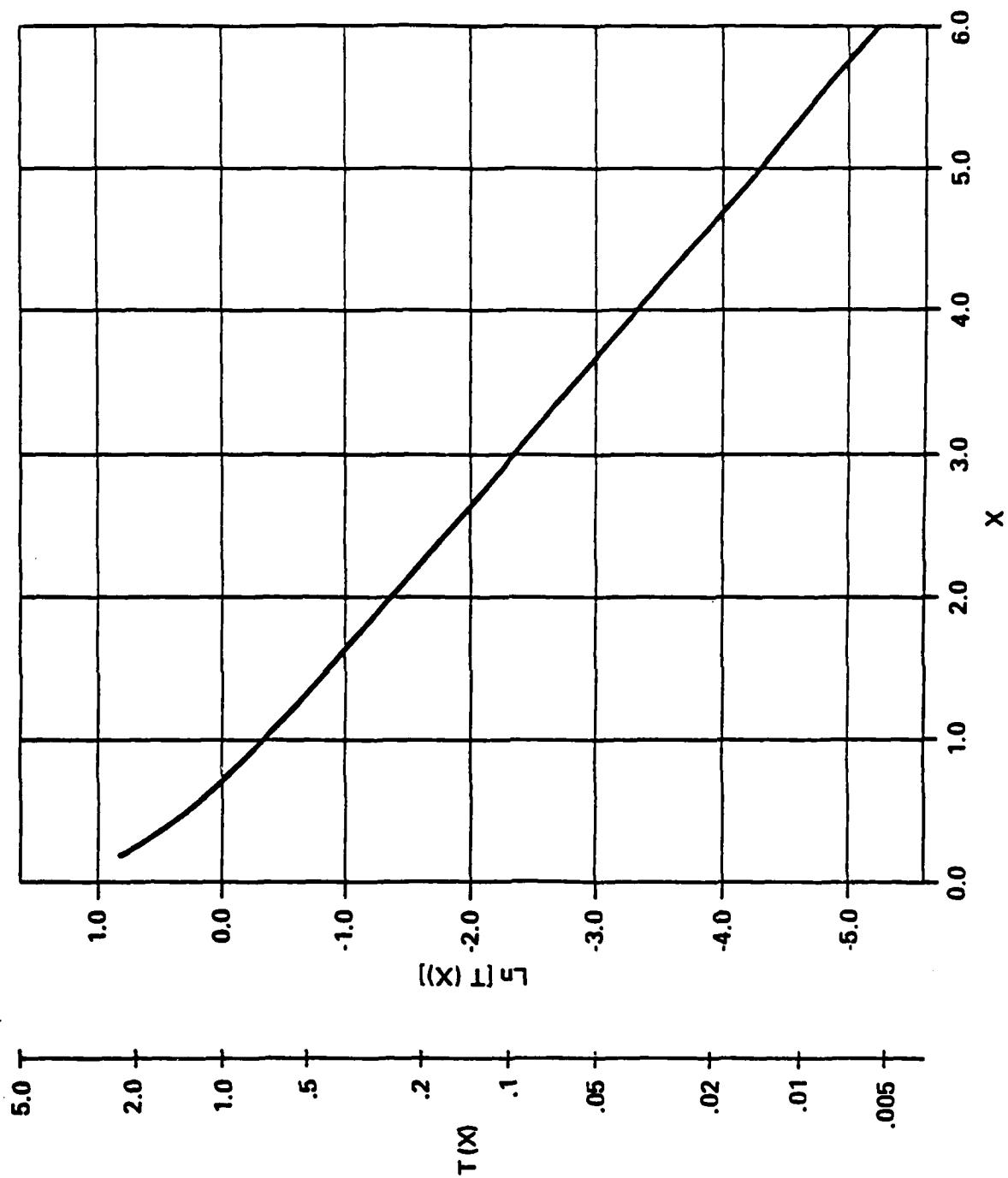


Figure 9

TABLE III

$\left(\frac{r_2}{r_1}\right)$	Segment Shape	B_1 (Kgauss)	$\frac{b_9}{b_1}$ (%)
2	trapezoid	5.42	9.5
2	rectangle	4.18	0.2
3	rectangle	5.66	0.01

A preliminary analysis of a helical wiggler design with $B_h = 2$ kilogauss and $\lambda = 5$ cm has been made. The first step was to investigate different configurations for the dipole ring. Table 3 gives the results for infinitely long (2D) rings assuming $B_r = 8.7$ kilogauss. For mechanical reasons, a design with rectangular pieces is preferable as this allows for mechanical support of the pieces and the possibility of moving the pieces to tune out harmonic errors, as will be discussed below.

Figure 10 shows a helical wiggler design concept with the following parameters.

$$B_r K_1 \frac{\sin \frac{\pi}{J}}{\frac{\pi}{J}} = (8.7) (.9) (.9)$$

$$x_1 = \frac{2\pi r_1}{\lambda} = \frac{2\pi (1.5)}{5} = 1.85$$

$$T(x_1) = .3$$

$$x_2 = \frac{2\pi (4.5)}{5} = 5.65$$

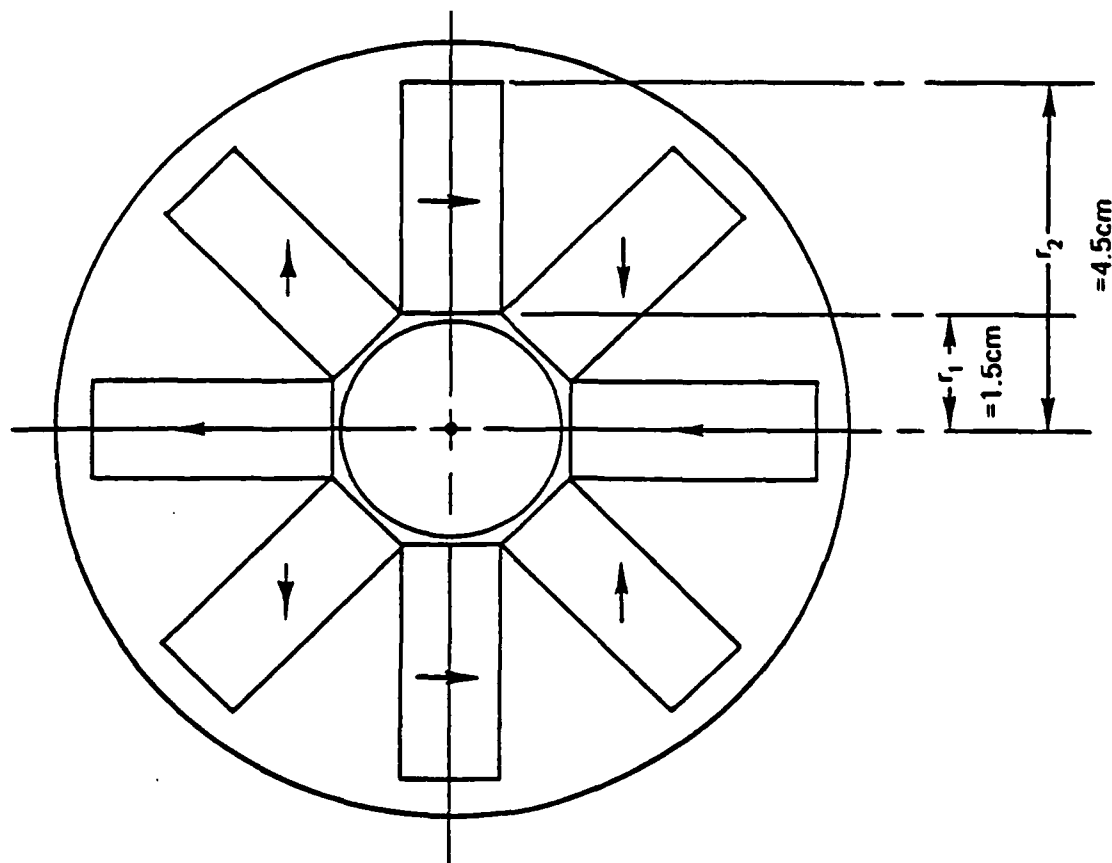
$$T(x_2) = 0.01$$

This gives a wiggler amplitude of

$$B_h = (8.7) (.9) (.9) (.29) = 2.04 \text{ Kgauss}$$

ORIENTATION OF RECTANGULAR REC MAGNETS IN HELICAL WIGGLER

FRONT VIEW OF RECTANGULAR MAGNETS IN DIPOLE RING



SIDE VIEW OF DIPOLE RINGS IN HELICAL WIGGLER

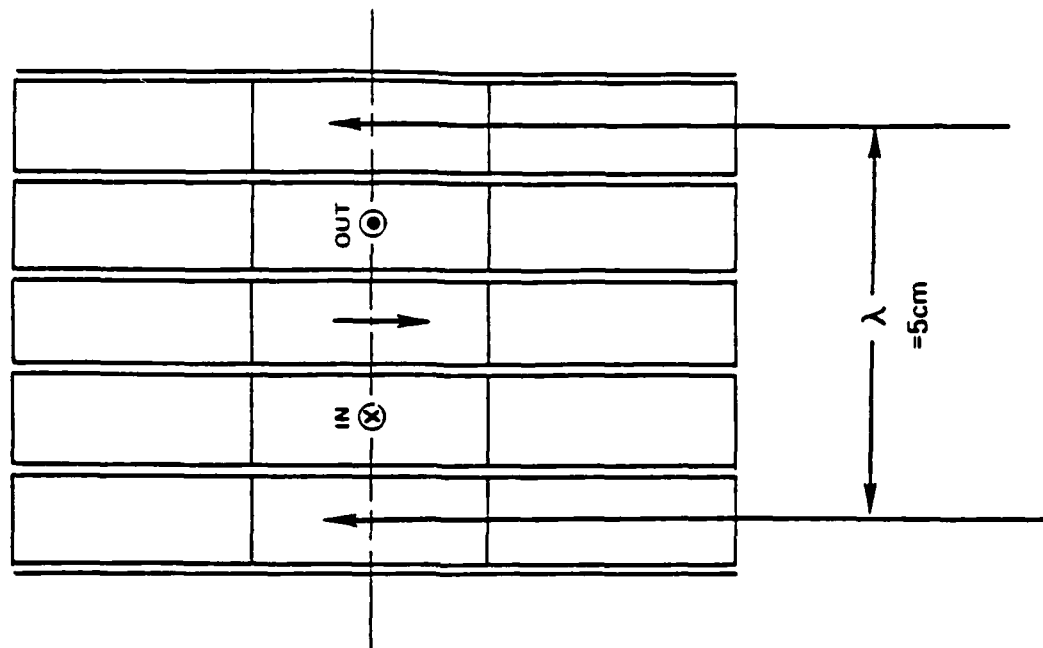


Figure 10

3. Dipole Ring Tuning: Although many REC multiple magnets have been built with no provisions for tuning the multipole field errors, the requirements on the uniformity of the magnet pieces are very stringent for high precision field distributions. A way to understand how a tuning procedure may be implemented, is to consider the field produced by an individual magnet block. In general a single block produces all harmonics which may be expressed as

$$B_x^S - iB_y^S = \sum_{n=1}^{\infty} C_n z^{n-1} \quad (E-8)$$

Let us call the block bisected by the x-axis in a multipole assembly the reference block, as shown in Figure 11. The C_n in (E-8) are produced by this block. The resultant fields produced by an assembly of M blocks in a symmetrical array are just the sum of the harmonics produced by a single block, i.e. b_n in (E-5) is equal to MC_n . Of course only certain n's are allowed according to (E-6) all other harmonics exactly canceling. The C_n for an arbitrarily shaped reference block may be derived by evaluating the following integral

$$C_n = \frac{B_r}{4\pi i} \int \frac{dz^*}{z^n} \quad (E-9)$$

where B_r is the complex representation of the residual induction. If the position of the reference block is perturbed, the change in the C_n can be calculated directly from (E-9). The result is

$$\Delta C_n = -n \Delta z C_{n+1} \quad (E-10)$$

The same relationship exists for every block in the assembly with a different absolute phase angle for each block.

The consequences of the analysis above are that by small perturbations of the position of the REC blocks in a multipole assembly, specific harmonic errors of given amplitude and phase (real and imaginary part) may be produced.

A particular multipole tuning procedure then could be implemented as follows. First, measure the amplitude and phase of each harmonic

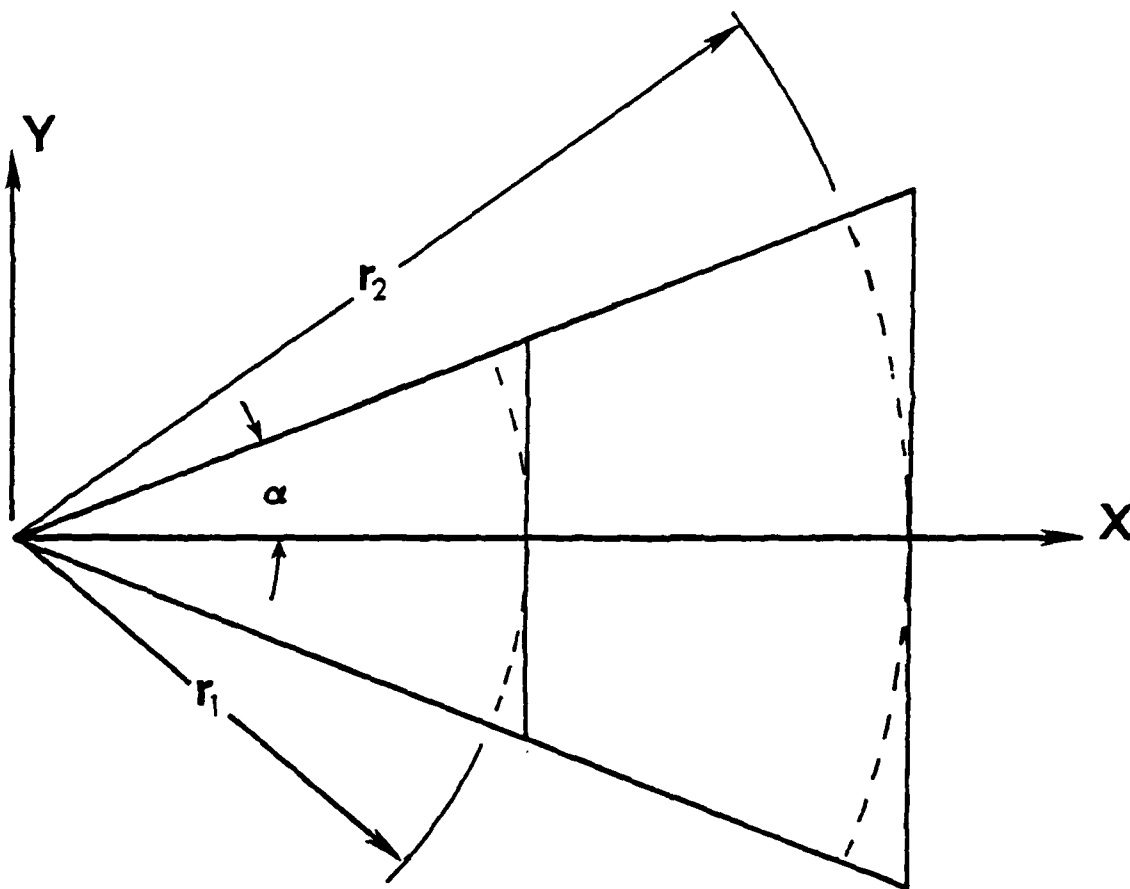


Figure 11

multipole field error. This can be done with harmonic multipole measuring equipment as described in reference 9. Second, calculate the set of magnet block radial perturbations which create the negative of the measured errors with the proper phase. Depending on the criterion which is chosen to reduce the field errors, one may wish to eliminate exactly a number of low order errors, or the strength of a larger number of multipole errors may be reduced by, for example a weighted least squares minimization procedure. In general it requires at least the radial movement of two magnet blocks to cancel one harmonic error, since the b_n are complex.

F. Accelerator Studies

The success of the two-stage FEL experiment will depend on the proper functioning of all equipment in the system. This includes the accelerator that supplies the beam. Beam current, pulse length, and voltage stability are critical factors in the experiment that are determined by the accelerator, and the amount of power that can be obtained from the FEL is also limited by the accelerator.

During the period covered by this report we have studied the adequacy of the present UCSB accelerator system for the two-stage FEL experiment. As a result of this work, we have identified areas in which accelerator improvements are necessary to insure the success of the two-stage FEL experiment and the usefulness of the experimental results for extrapolation to higher laser powers. We have also developed a conceptual design for a very high power FEL and identified technologies needed for this high power design that could be tested using the UCSB accelerator.

1. Deficiencies of the Present UCSB Accelerator: In the present UCSB electrostatic accelerator,¹⁰ the charge on the dome of the accelerator is provided by a pelletron charging chain capable of supplying 500 μ amp of input current. Initially the accelerator will operate with a 2-amp pulse. Electrons leaving the accelerator pass through the FEL amplifier and are directed back up the accelerator column where they are recaptured and reused. The charging current, therefore, is only needed to start up the accelerator and to compensate for system losses during operation.

If 99.975% of the electrons leaving the dome of the accelerator were recollected, an average current of 2 amp could be achieved. It is not expected, however, that collection efficiency will be this good. Therefore, the accelerator will be operated in a pulsed mode. As a pulse of constant current is emitted from the accelerator, the charge on the dome will be depleted and the accelerating voltage will begin to fall or droop. The length of the pulse will be a function of the droop that can be tolerated in the FEL. Droop voltage for a 2-amp beam in the UCSB accelerator is plotted as a function of pulse length for a number of assumed current loss rates in Figure 12. For a single-stage long-wavelength FEL several kilovolts of droop could be tolerated before the laser ceases to produce gain at the desired frequency. For the second stage of a two-stage FEL, the maximum droop that could be tolerated would be a few hundred volts. Even if a voltage droop could be "tolerated", interpretation of the data from an experiment with voltage droop would be very complicated and difficult to extrapolate to high power operation.

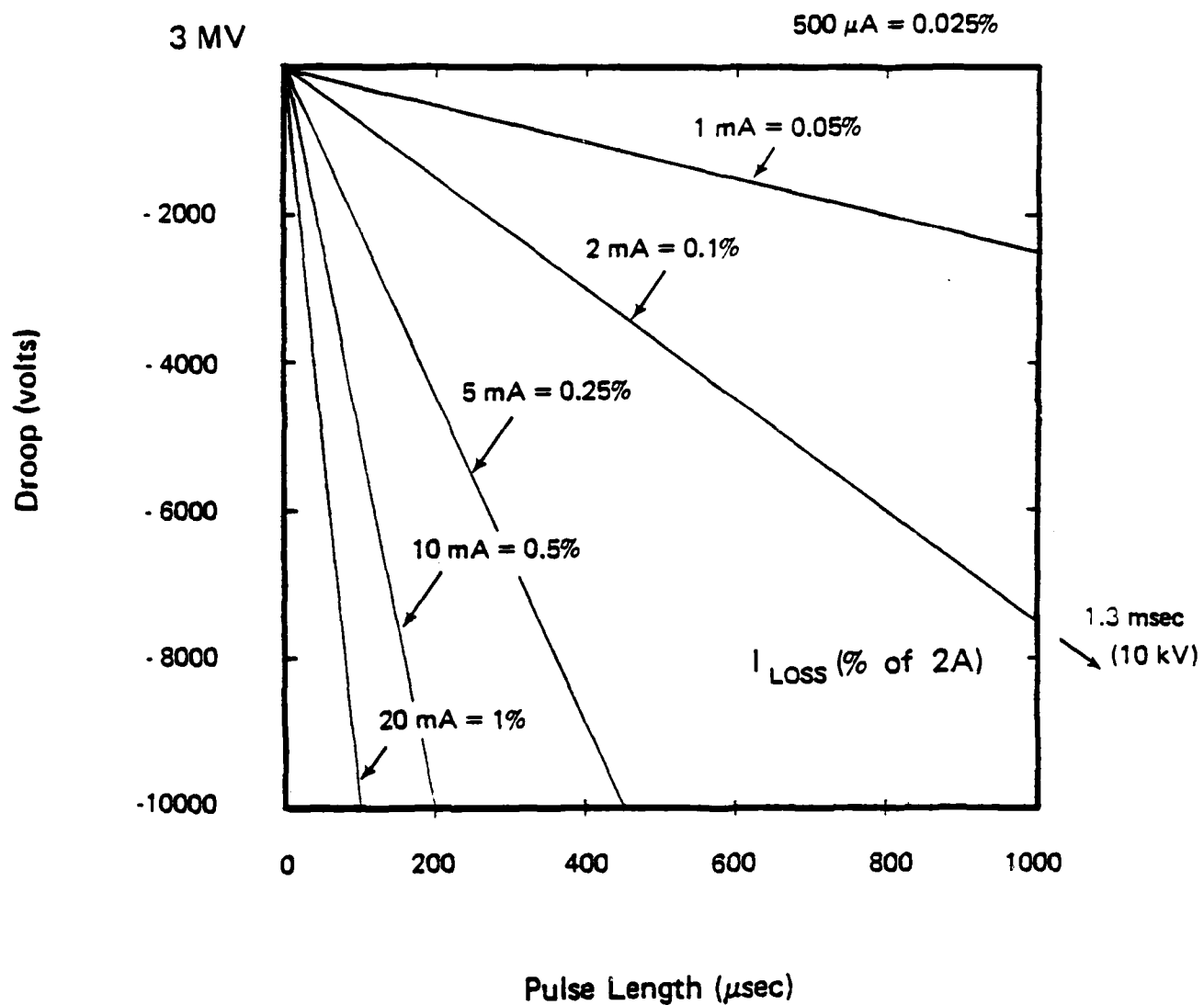
The length of the electron pulse is determined by the rate at which charge is lost by the dome of the accelerator. For the present system a pulse length of 75 μ sec, determined by the amount of droop that could be tolerated in the first stage, has been predicted for operation at 2 amp. If the electron current is increased by a factor of 10, it is anticipated that the pulse length will be decreased by at least this factor.

In a free electron laser oscillator, a finite amount of time is required for the laser pulse to build up from spontaneous emission to a saturation value at which the gain in the laser just covers optical system losses. The time required for this buildup in the Stanford FEL is a minimum of a few tens of microseconds. For both the second stage laser field and the first stage pump field to build up from spontaneous emission will probably require at least several tens of microseconds. It is, therefore, not certain that with the present accelerator design the electron pulse will be long enough to permit the laser pulse to reach its predicted saturation value.

We assume that a maximum effort will be made to lengthen the electron pulses by reducing beam losses. The predicted 75 μ sec pulse

EFFECT OF CURRENT LOSS ON PULSE

LENGTH ($I_{CH} = 500 \mu A$)



$$\frac{\Delta V}{\Delta t} = \frac{I_{LOSS} - I_{CH}}{C}$$

$C = 200 \mu\mu f$

Figure 12

length for a 2-amp beam and 7.5 μ sec pulse length for a 20-amp beam are obtained by assuming these efforts will be successful. In order to increase the pulse length further, it will be necessary to correct for the voltage droop that limits the pulse length.

2. Control of Voltage Droop: The rates for charging and discharging the dome of the accelerator are given by

$$K_C = \frac{I_C}{C} \quad \text{and} \quad K_D = \frac{I_L}{C} \quad (F-1)$$

where I_C is the charging current, I_L is the current that is not recollected by the accelerator, and C is the capacitance of the dome. The net rate of discharging is given by

$$K_D - K_C = \frac{\Delta V}{\Delta t} = \frac{I_L - I_C}{C} \quad (F-2)$$

where ΔV is the voltage drop of the terminal. For the UCSB accelerator current losses during the electron pulse are much greater than the charging current, i.e., $I_L \gg I_C$.

Without correction for voltage droop, the electron pulse length is determined by the voltage droop that can be accepted. This discharge time will be given by

$$\Delta t_D = \frac{\Delta V}{K_D} \quad (F-3)$$

The time required to recharge the terminal between pulses is given by

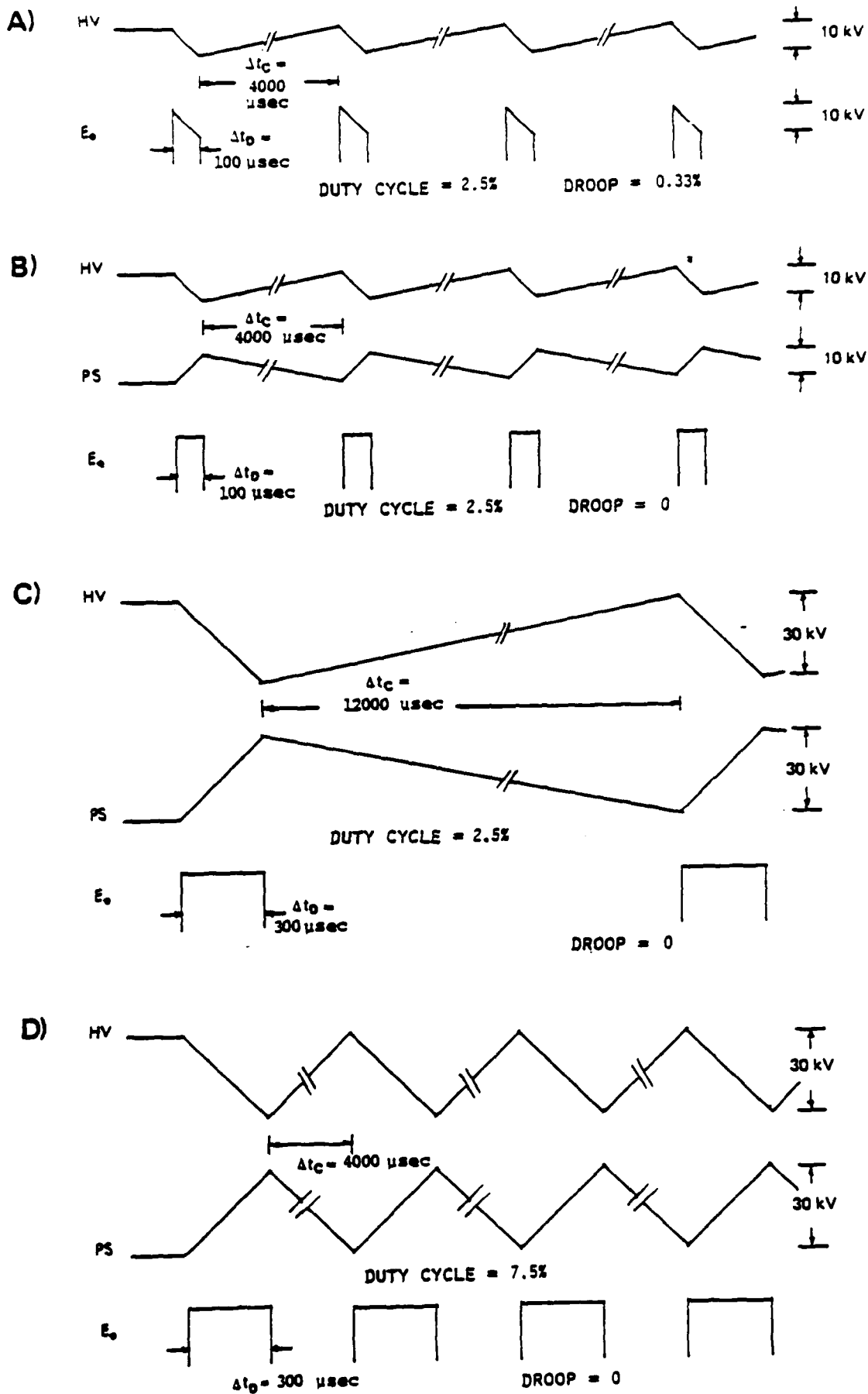
$$\Delta t_C = \frac{\Delta V}{K_C} \quad (F-4)$$

and the duty cycle is

$$D = \frac{\Delta t_D}{\Delta t_D + \Delta t_C} = \frac{I_C}{I_L} \quad (F-5)$$

For example, if $I_C = 500 \mu\text{amp}$, $I_L = 20 \text{ mamp}$ and $C = 200 \text{ pF}$, then $K_C = 2.5 \text{ V}/\mu\text{sec}$ and $K_D = 100 \text{ V}/\mu\text{sec}$. If we allow a ΔV of 10 kV then the pulse length Δt_D is 100 μsec , the recharging time is 4000 μsec and the duty cycle is 0.025. This is shown schematically in Figure 13(a).

FIGURE 13



The voltage droop can be eliminated by providing a voltage ramp to accelerate the electrons by exactly the amount that the terminal voltage is reduced (Figure 13b). This voltage ramp would be provided by a power supply in the dome of the accelerator that ramps the voltage of the electron gun and electron collector relative to the dome during the current pulse. The power needed to operate the power supply would be provided by the generator in the dome. Any change in beam focusing produced by the accelerating gap could be corrected using variable voltage Einzel lenses.

When the voltage droop has been cancelled, the pulse length is no longer determined by the maximum droop the FEL can accept, but by the maximum droop the ramped power supply can correct. The latter may be greater by a factor of a few than the former. The size of the power supply and the breakdown voltage for the accelerating gap limit the droop that can be corrected to about 30 keV. If the charging current remains constant, there will be no change in duty cycle, so that the time required to recharge the terminal increases as the electron pulse length is increased (Figure 13c). Increasing the charging current will have practically no effect on the electron pulse length when $I_L \gg I_C$, but will increase the duty cycle (Figure 13d).

3. Control of Voltage Ripple: The pelletron chain, which is used to transfer charge to the HV terminal, is charged by induction. It can be charged negatively at the accelerator base, and positively at the terminal to double the net charge transferred. Ripple is caused by imbedded charge which is not transferred in the charge-discharge process. The amount of imbedded charge can vary with time. The ripple voltage has two main frequency components: one at 400 Hz arising from the charging variations of individual pelletron links, and one at a much lower frequency, ~ 3 Hz, corresponding to the complete chain cycle time. For a completely unregulated machine, the amplitude of the ripple is on the order of kilovolts.

Conventional stabilization methods utilize a coarse and fine control to minimize ripple. The coarse control can only control ripple to about 1 part in 10^3 of the total accelerator voltage, whereas the fine control usually reduces the ripple to 1 part in 10^4 or less. The state-of-the-art in ripple control is a few parts in 10^5 . Coarse control for the

UCSB machine utilizes a generating voltmeter to detect voltage changes on the terminal and a corona discharge to modulate a leakage charge for correction.

For fine control of ripple the signal from an energy sensitive diagnostic, such as a stabilized analyzing magnet and slit detector, could be used to modulate the voltage on the same power supply already being used to correct for voltage droop.

4. Accelerator Power System Limitations: Although the 20 kw generator and associated motor and power supplies in the UCSB accelerator are adequate at present, they may not be able to provide adequate power when the beam current is increased. If 1% of the electron energy is converted to photon energy in a 2-amp, 3-MeV beam, the instantaneous power that must be supplied is 60 kw. For a 20-amp beam this will increase to 600 kw. Because the gain in both the pump and laser fields will be higher in the 20 amp case, more than 1% of the electron energy may be converted to photon energy when the system reaches its equilibrium operating point. In order to accommodate this higher energy loss it will be necessary to increase the voltage on the electron gun and increase the voltage spread that the collector can accept. Correction for voltage droop will permit increasing the electron pulse length and hence the time over which peak power is drawn from the power supplies in the dome. This will impact the amount of energy that must be stored to provide for peak power loading.

5. Design of an Accelerator for a High Power FEL: Even if the voltage stability of the UCSB accelerator is improved it will not be capable of driving a high-average-power FEL. One reason for this is that the total power that can be generated in both the pump and the laser fields of the FEL cannot exceed the generator power in the dome of the accelerator. In the UCSB device, there is only a 20 kw generator in the dome of the accelerator.

Other factors also limit the average power that can be obtained using the UCSB accelerator design. When operating in a pulsed mode, the laser pulse must build up from spontaneous emission for each pulse. Therefore, the laser will at best operate at its saturation power value

for only a fraction of the time the electron pulse is on, and the electron pulse will be on only a small fraction of the time between pulses. The low duty cycle is the result both of inadequate charging current to permit continuous operation and inadequate power to provide energy to the electrons for continuous operation.

At KMSF we have developed a design concept for an electrostatic accelerator that could provide both the input current and the power needed to operate a high-average-power FEL. In the accelerator design we are considering, an insulated core transformer (ICT) is used to provide the input current to the dome of the accelerator. An ICT could provide a few tens of milliamperes of input current at voltages of a few MeV directly to the dome of the accelerator with 90% wallplug efficiency. A diagram of an accelerator incorporating an ICT is shown in Figure 14.

To provide adequate power for operating the FEL, four samarium cobalt permanent magnet generators, each of which is rated at 250-400 kw and weighs 120 lb., are located in the dome of the accelerator. The generators are powered by two 800 hp motors with counter-rotating drive shafts located outside the accelerator. The insulating drive shafts may be operated directly using a ferro-fluidic feedthrough, as shown in Figure 14, or using a fluid-driven turbine to transmit power to the drive shaft inside the accelerator. The permanent magnet generators operate at 20,000 rpm and a gear box would be used to operate the drive shaft at 2000 rpm. The overall efficiency of producing power in the dome of the accelerator is estimated to be about 80%.

All of the equipment needed to build this accelerator is commercially available. The major technological problem that needs to be demonstrated is efficient recollection of the high current electron beam. Also, operation of the generators and the entire power transmission assembly must be demonstrated inside an electrostatic accelerator.

The voltage of the ICT has a periodic ripple of about 1% at 360 Hz. This ripple could be reduced by a factor of 1000 using the filter circuit shown in Figure 15. It is necessary in constructing this filter that the accelerator and ICT column domes remain separate. This is shown in Figure 14. Further correction for small, nonperiodic voltage ripple could be accomplished with a beam energy analyzer and feedback system.

COLUMN CROSS-SECTION

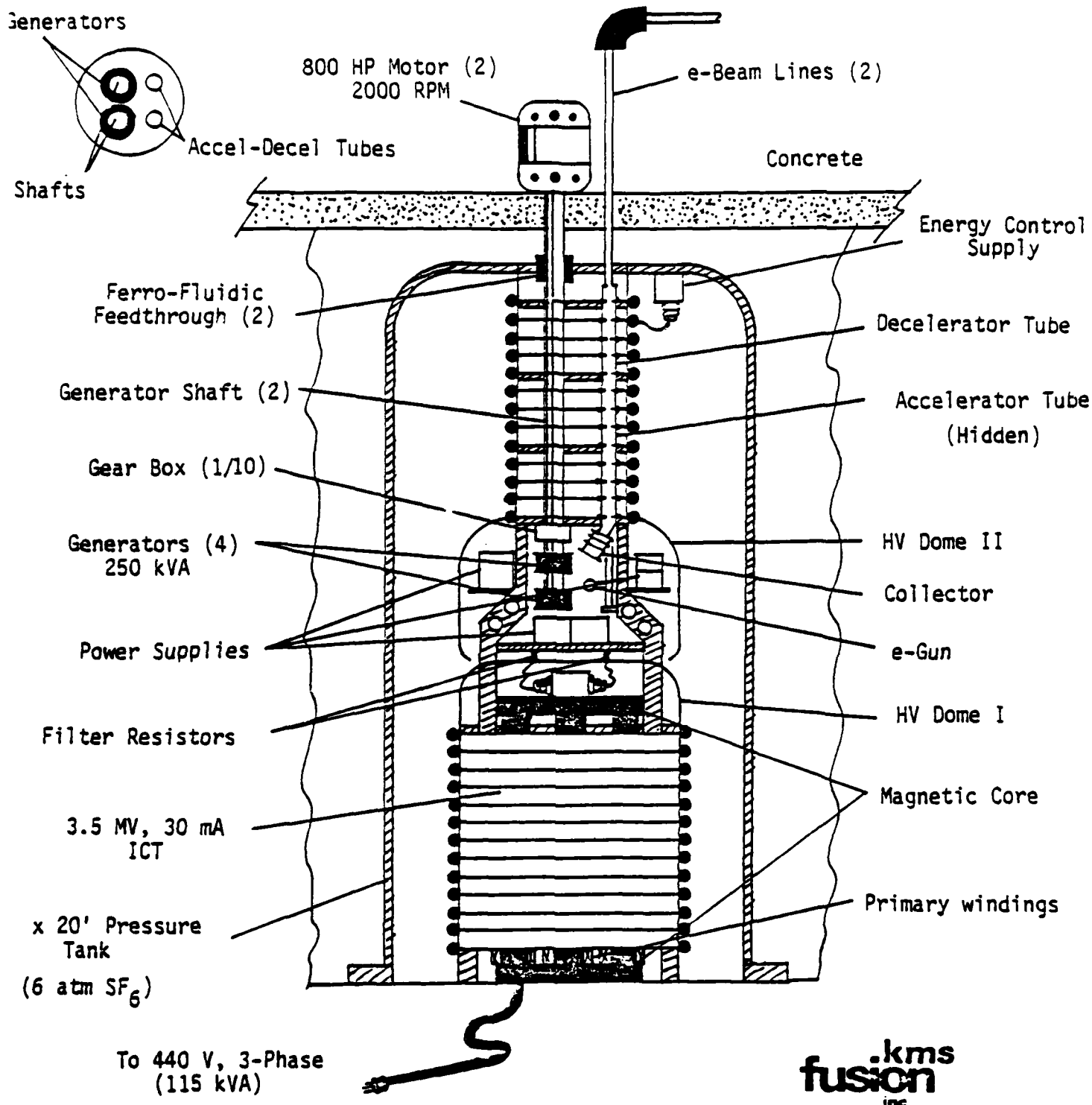
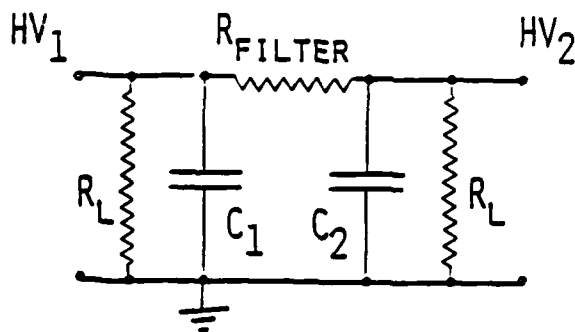


Figure 14

ICT FILTER CIRCUIT



ASSUMPTIONS

- ★ 360 Hz (3-PHASE, FWR) WITH 1% RIPPLE
- ★ 60 Hz WITH 0.02% RIPPLE
- ★ $C_1 = C_2 = 200 \mu\text{F}$.
- ★ $R_L = 3500 \text{ M}\Omega$ (1 MA BLEEDER CURRENT)

RESULTS

- ★ $R_{\text{FILTER}} = 200 \text{ M}\Omega$
- ★ RIPPLE (360 Hz) IS 1 IN 10^5
- ★ RIPPLE (60 Hz) IS 1 IN 10^5
- ★ POWER DISSIPATION IS $30 \text{ MA} \times 35 \text{ kV} \cong 1 \text{ kW}$

Figure 15

As an example, we consider an accelerator with 3.5-MeV, 20-amp DC beam that is recirculated with 99.9% charge collection efficiency. The ICT makes up the 20-mamp current loss. If an average of 1.4% of the electron beam energy is converted to photon energy in the FEL, 1 MW of power must be supplied to the recollected electron beam by the generators in the dome of the accelerator. Since the ICT is only 90% efficient and the generator system is $\sim 80\%$ efficient, heat will be generated in the accelerator tank that would have to be removed by an active cooling system.

Although the accelerator column and ICT are shown in tandem in Figure 14, it would also be possible to locate them along side each other for a more compact design (Figure 16).

G. Multidimensional FEL Simulation Code

The one dimensional resonant particle and multiparticle simulation codes that have been developed at KMSF have enabled us to obtain general scaling relations for the two-stage FEL as well as more detailed information about optimization of laser gain and conversion efficiency during the pulse buildup. These codes cannot, however, provide information about the mode structure of the optical beam, beam quality, or output coupling, or provide information about the actual electron trajectories in the interaction region. The 1-D codes do not take the radial profile of the electron beam and optical beam into account, and therefore provide only approximate values for laser gain and conversion efficiency, which are not sufficiently accurate for detailed comparison with experiment.

To improve our capability to model a two-stage FEL experiment we have developed two and three dimensional computer simulation codes and a two dimensional resonant cavity design code. In this section we will present the general three dimensional formalism for propagation of the laser field and the electromagnetic pump field in the FEL. The method of solution of the wave equation using fast Fourier transforms in a Cartesian coordinate system will be described, and then it will be shown how this same formalism can be applied to a system in which cylindrical coordinates are employed.

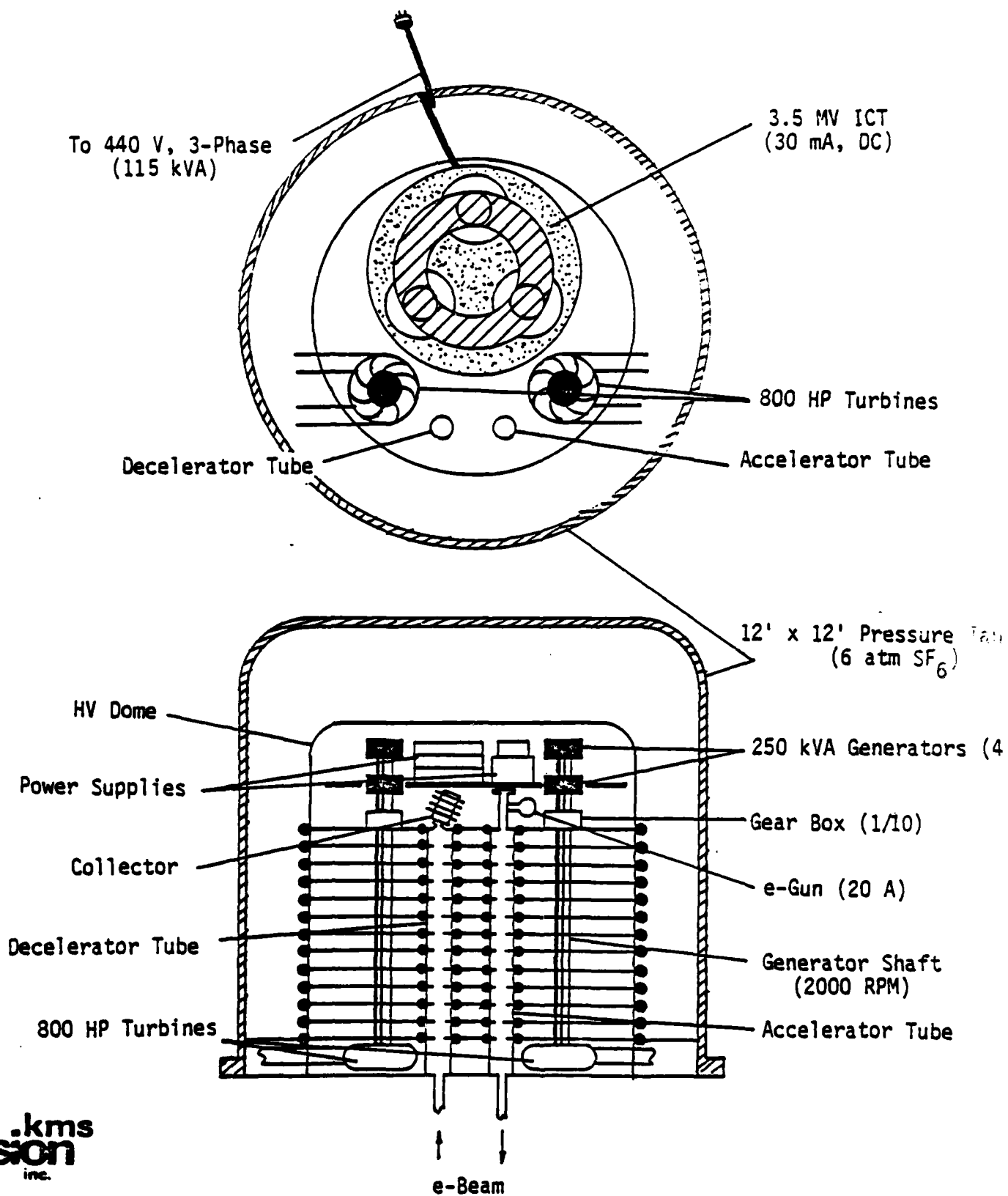


Figure 16

In the development of the multidimensional codes a number of subtle points had to be considered to insure that the codes would be both fast and accurate. In particular, it had to be shown that the incremental solution of the wave equation would be unitary, so that no artificial gains or losses would be introduced in the absence of a driving source term. To solve the wave equation in cylindrical coordinates using fast Fourier transforms, a transformation is made on the radial part of the wave equation.

Since the experiment we are planning will have cylindrical symmetry, a 2-D code has been written which assumes cylindrical symmetry. To use the code for design optimization of an FEL amplifier it is necessary to know what effect varying an axial electric field (or equivalently tapering the period of a wiggler magnet) would have on the resonant phase of the ponderomotive wave as a function of radial position. This is determined by developing a description of the electron dynamics for the resonant particle in the 2-D code.

1. The Three Dimensional Wave Equation: The propagation of an electromagnetic wave in space is determined by the three dimensional Maxwell wave equation

$$\left(\nabla^2 - \frac{1}{c^2} \frac{\partial^2}{\partial t^2}\right) \vec{A} = -\mu_0 \vec{J} \quad (G-1)$$

We will solve this equation for the general case in which both a laser field \vec{A}_L and an electromagnetic pump field \vec{A}_p combine to form a ponderomotive force which acts on the electrons.

The currents used in the solution of the wave equation in any time interval, Δt , are obtained from the motion of the electrons during that time interval. The solution of the wave equations in the 1-D case was made simpler by using two assumptions: 1) the slowly varying field approximation which allowed linearization of the left hand side (LHS) of the wave equation, and 2) the proper choice of propagation vectors on which to project the wave equation. The latter allowed the separation of the differential equations for the amplitude and phase of the fields and simultaneously provided exact analytic forms for the single-particle currents (the RHS of the wave equation). It will be shown that using

these assumptions the wave equation can be written in the form

$$[\nabla_{\perp}^2 + 2ik_L (\frac{\partial}{\partial z} + \frac{1}{c} \frac{\partial}{\partial t})] \vec{A}_L = -\mu_0 \vec{J}_{\perp} \quad (G-2)$$

where k_L is the longitudinal component of the wave number for the laser field and \vec{J}_{\perp} is the perpendicular component of the electron current. Likewise for the pump field

$$[\nabla_{\perp}^2 + 2ik_p (\frac{\partial}{\partial z} - \frac{1}{c} \frac{\partial}{\partial t})] \vec{A}_p = -\mu_0 \vec{J}_{\perp} \quad (G-3)$$

In the 3-D case, we generalize the vector potentials to have amplitude and phases that depend on x, y, z and t but which propagate only in the z -direction. The latter property suggests we find a way to represent the potentials used in the wave equation so that the evolution of the amplitude and phase part can be handled separately from the propagation part.

The vector potentials for the laser field and the electromagnetic pump field are given by

$$\vec{A}_L = A_L(\vec{x}, t) [\hat{x} \cos(k_L z - \omega_L t + \phi_L) - \hat{y} \sin(k_L z - \omega_L t + \phi_L)] \quad (G-4)$$

and

$$\vec{A}_p = -A_p(\vec{x}, t) [\hat{x} \cos(k_p z + \omega_p t + \phi_p) + \hat{y} \sin(k_p z + \omega_p t + \phi_p)] \quad (G-5)$$

where $\phi_L = \phi_L(\vec{x}, t)$, $\phi_p = \phi_p(\vec{x}, t)$.

We now rewrite these in a form suitable for separating the z, t propagation part from the x, y part.

$$\vec{A}_L = A_L(\vec{x}, t) \frac{1}{2} [e^{i(k_L z - \omega_L t)} e^{i\phi_L}] (\hat{x}, i\hat{y}) + c.c. \quad (G-6)$$

or

$$\vec{A}_L = \text{Re} \{ A_L(\vec{x}, t) [e^{i(k_L z - \omega_L t)} e^{i\phi_L}] (\hat{x}, i\hat{y}) \}. \quad (G-7)$$

Similarly,

$$\vec{A}_p = -\text{Re} \{ A_p(\vec{x}, t) [e^{i(k_p z + \omega_p t)} e^{i\phi_p}] (\hat{x}, -i\hat{y}) \}. \quad (G-8)$$

Note that

$$\begin{aligned}
 e^{i(k_L z - \omega_L t)} (\hat{x}, i\hat{y}) &= [\hat{x} \cos(k_L z - \omega_L t) - \hat{y} \sin(k_L z - \omega_L t)] \\
 &\quad + i [+ \hat{x} \sin(k_L z - \omega_L t) + \hat{y} \cos(k_L z - \omega_L t)] \\
 &= \hat{e}_{1_L} - i\hat{e}_{2_L}
 \end{aligned} \tag{G-9}$$

where

$$\hat{e}_{1_L} \equiv \hat{x} \cos(k_L z - \omega_L t) - \hat{y} \sin(k_L z - \omega_L t) \tag{G-10}$$

and

$$\hat{e}_{2_L} \equiv -\hat{x} \sin(k_L z - \omega_L t) - \hat{y} \cos(k_L z - \omega_L t). \tag{G-11}$$

Also note that

$$e^{i(k_P z + \omega_P t)} (\hat{x}, -i\hat{y}) = -(\hat{e}_{1_P} - i\hat{e}_{2_P}) \tag{G-12}$$

where

$$\hat{e}_{1_P} \equiv -\hat{x} \cos(k_P z + \omega_P t) - \hat{y} \sin(k_P z + \omega_P t) \tag{G-13}$$

and

$$\hat{e}_{2_P} \equiv \hat{x} \sin(k_P z + \omega_P t) - \hat{y} \cos(k_P z + \omega_P t). \tag{G-14}$$

We further define

$$\underline{A}_L \equiv A_L(\vec{x}, t) e^{i\phi_L} \quad \hat{f}_L \equiv \hat{e}_{1_L} - i\hat{e}_{2_L} \tag{G-15,16}$$

$$\underline{A}_P \equiv A_P(\vec{x}, t) e^{i\phi_P} \quad \hat{f}_P \equiv -(\hat{e}_{1_P} - i\hat{e}_{2_P}) \tag{G-17,18}$$

\underline{A}_L , \underline{A}_P carry the amplitude and phase shift information which depend on (\vec{x}, t) and the vectors \hat{f}_L , \hat{f}_P depend only on (z, t) . Then

$$\vec{A}_L = \text{Re}[\underline{A}_L \hat{f}_L] = 1/2 \underline{A}_L \hat{f}_L + \text{c.c.} \tag{G-19}$$

and

$$\vec{A}_p = -\text{Re}[\underline{A}_p \hat{f}_p] = -1/2 \underline{A}_p \hat{f}_p + \text{c.c.} \quad (\text{G-20})$$

Defining

$$\alpha_L = (k_L z - \omega_L t), \quad (\text{G-21})$$

and

$$\Psi_0 \equiv \alpha_L + \alpha_p = (k_L + k_p)z - (\omega_L + \omega_p)t \quad (\text{G-22})$$

it can be shown that

$$-e_{1L} \cdot e_{1p} = e_{2L} \cdot e_{2p} = \cos \Psi_0 \quad \hat{e}_{1L} \cdot \hat{e}_{1L} = 1, \text{ etc.} \quad (\text{G-23,24})$$

$$e_{1L} \cdot e_{2p} = e_{2L} \cdot e_{1p} = \sin \Psi_0 \quad \hat{e}_{1L} \cdot \hat{e}_{2L} = \hat{e}_{1p} \cdot \hat{e}_{2p} = 0. \quad (\text{G-25,26})$$

It can also be shown that

$$\hat{f}_L \cdot \hat{f}_L^* = 2, \quad \hat{f}_p \cdot \hat{f}_p^* = 2 \quad (\text{G-27,28})$$

$$\hat{f}_L \cdot \hat{f}_p^* = 0, \quad \hat{f}_p \cdot \hat{f}_L^* = 0 \quad (\text{G-29,30})$$

and

$$\hat{f}_p^* \cdot \hat{f}_L^* = 2e^{-i\Psi_0}, \quad (\text{G-31})$$

Also,

$$\hat{f}_L^2 = \hat{f}_p^2 = (\hat{f}_L^*)^2 = (\hat{f}_p^*)^2 = 0. \quad (\text{G-32})$$

The result of this formalism is that the complex form of the fields can be written as projections of the real vector potentials onto the complex vectors:

$$\underline{A}_L = \vec{A}_L \cdot \hat{f}_L^*, \quad \underline{A}_p = -\vec{A}_p \cdot \hat{f}_p^*. \quad (\text{G-33,34})$$

Since $\frac{\partial}{\partial z} (\hat{e}_1)_{L,p} = k_{L,p} (\hat{e}_2)_{L,p}$ and $\frac{\partial}{\partial z} (\hat{e}_2)_{L,p} = -k_{L,p} (\hat{e}_1)_{L,p}$,

then:

$$\frac{\partial}{\partial z} \hat{f}_L = ik_L \hat{f}_L, \quad \frac{\partial^2}{\partial z^2} \hat{f}_L = -k_L^2 \hat{f}_L \quad (G-35,36)$$

$$\frac{\partial}{\partial z} \hat{f}_p = ik_p \hat{f}_p, \quad \frac{\partial^2}{\partial z^2} \hat{f}_p = -k_p^2 \hat{f}_p \quad (G-37,38)$$

Similarly

$$\frac{\partial}{\partial t} \hat{f}_L = -i\omega_L \hat{f}_L, \quad \frac{\partial^2}{\partial t^2} \hat{f}_L = -\omega_L^2 \hat{f}_L \quad (G-39,40)$$

$$\frac{\partial}{\partial t} \hat{f}_p = i\omega_p \hat{f}_p, \quad \frac{\partial^2}{\partial t^2} \hat{f}_p = -\omega_p^2 \hat{f}_p. \quad (G-41,42)$$

Evaluation of the LHS of the Wave Equation

Next we evaluate $\square^2 A$ for each field, where

$$\square^2 \equiv \left[\nabla_{\perp}^2 + \frac{\partial^2}{\partial z^2} - \frac{1}{c^2} \frac{\partial^2}{\partial t^2} \right]. \quad (G-43)$$

For the laser field:

$$\begin{aligned} \left[\frac{\partial^2}{\partial z^2} - \frac{1}{c^2} \frac{\partial^2}{\partial t^2} \right] \left(\frac{1}{2} A_L \hat{f}_L \right) &= \left[\frac{1}{2} \hat{f}_L \frac{\partial^2 A_L}{\partial z^2} + \frac{\partial A_L}{\partial z} \frac{\partial \hat{f}_L}{\partial z} + \frac{1}{2} A_L \frac{\partial^2 \hat{f}_L}{\partial z^2} \right] \\ &\quad - \frac{1}{c^2} \left[\frac{1}{2} \hat{f}_L \frac{\partial^2 A_L}{\partial t^2} + \frac{\partial A_L}{\partial t} \frac{\partial \hat{f}_L}{\partial t} + \frac{1}{2} A_L \frac{\partial^2 \hat{f}_L}{\partial t^2} \right] \\ &= ik_L \hat{f}_L \left[-\frac{\partial A_L}{\partial z} + \frac{1}{c} \frac{\partial A_L}{\partial t} \right] \end{aligned} \quad (G-44)$$

where we have assumed $k_L = \omega_L/c$ and $\frac{\partial^2 A_L}{\partial z^2} = \frac{\partial^2 A_L}{\partial t^2} = 0$, that is, the fields are slowly varying in the propagation direction. Then

$$\square^2 \hat{A}_L = \left[\frac{1}{2} \nabla_{\perp}^2 + ik_L \left(\frac{\partial}{\partial z} + \frac{1}{c} \frac{\partial}{\partial t} \right) \right] A_L \hat{f}_L + c.c. = -\mu_0 J_{\perp} \quad (G-45)$$

or

$$\text{Re} \left\{ \left[\frac{1}{2} \nabla_{\perp}^2 + ik_L \left(\frac{\partial}{\partial z} + \frac{1}{c} \frac{\partial}{\partial t} \right) \right] A_L \hat{f}_L \right\} = -\frac{\mu_0}{2} J_{\perp}. \quad (G-46)$$

$$D_L \equiv \left[\frac{1}{2} \nabla_L^2 + ik_L \left(\frac{\partial}{\partial z} + \frac{1}{c} \frac{\partial}{\partial t} \right) \right] \quad (G-47)$$

then

$$(D_L A_L) \hat{f}_L + (D_L A_L)^* \hat{f}_L^* = -\mu_0 J_L. \quad (G-48)$$

To eliminate \hat{f}_L from the LHS, project both sides onto \hat{f}_L^* :

$$(D_L A_L) \hat{f}_L \cdot \hat{f}_L^* + (D_L A_L)^* (\hat{f}_L^*)^2 = -\mu_0 J_L \cdot \hat{f}_L^* \quad (G-49)$$

or

$$D_L A_L = -\frac{\mu_0}{2} J_L \cdot \hat{f}_L^*. \quad (G-50)$$

Similarly, for the pump field:

$$\text{Re} \left\{ \left[\frac{1}{2} \nabla_L^2 + ik_p \left(\frac{\partial}{\partial z} - \frac{1}{c} \frac{\partial}{\partial t} \right) \right] A_p \hat{f}_p \right\} = \frac{\mu_0}{2} \vec{J}_L. \quad (G-51)$$

and

$$D_p A_p = \frac{\mu_0}{2} \vec{J}_L \cdot \hat{f}_p^*. \quad (G-52)$$

Evaluation of the RHS of the Wave Equation

We look now at the form of the currents

$$J_L = \sum_i ec \beta_{Li} \quad (G-53)$$

where

$$\vec{\beta}_{Li} = \frac{1}{\gamma_i} \left(\frac{\vec{p}_{Li}}{mc} - \frac{e\vec{A}}{mc} \right), \quad (G-54)$$

$$\vec{A} = \vec{A}_L + \vec{A}_p, \quad (G-55)$$

and the sum is taken over all the electrons in a ponderomotive wavelength. Using (G-55), (G-33), (G-20), (G-29), and (G-31) it can be shown that

$$\vec{A} \cdot \hat{f}_L^* = \vec{A}_L - \vec{A}_p^* e^{-i\psi_0} \quad (G-56)$$

Similarly

$$\vec{A} \cdot \hat{f}_p^* = \underline{A}_L^* e^{-i\psi_0} - \underline{A}_p. \quad (G-57)$$

With these results

$$\vec{J}_L \cdot \hat{f}_L^* = \frac{e}{m} \sum_i \left(\frac{\vec{p}_{Li}}{\gamma_i} \cdot \hat{f}_L^* - \frac{e}{\gamma_i} [\underline{A}_L - \underline{A}_p^* e^{-i\psi_{0i}}] \right) \quad (G-58)$$

and

$$\vec{J}_L \cdot \hat{f}_p^* = \frac{e}{m} \sum_i \left(\frac{\vec{p}_{Li}}{\gamma_i} \cdot \hat{f}_p^* - \frac{e}{\gamma_i} [-\underline{A}_p + \underline{A}_L^* e^{-i\psi_{0i}}] \right). \quad (G-59)$$

Finally, the linearized wave equations for the pump and laser fields are given by

$$\left[\frac{1}{2} \nabla_L^2 + ik_L \left(\frac{\partial}{\partial z} + \frac{1}{c} \frac{\partial}{\partial t} \right) \right] \underline{A}_L = -\frac{\mu_0}{2} \frac{e}{m} \sum_i \left[\frac{\vec{p}_{Li}}{\gamma_i} \cdot \hat{f}_L^* - \frac{e}{\gamma_i} (\underline{A}_{Li} - \underline{A}_{pi}^* e^{-i\psi_{0i}}) \right] \quad (G-60)$$

and

$$\left[\frac{1}{2} \nabla_L^2 + ik_p \left(\frac{\partial}{\partial z} - \frac{1}{c} \frac{\partial}{\partial t} \right) \right] \underline{A}_p = \frac{\mu_0}{2} \frac{e}{m} \sum_i \left[\frac{\vec{p}_{Li}}{\gamma_i} \cdot \hat{f}_p^* - \frac{e}{\gamma_i} (-\underline{A}_{pi} + \underline{A}_{Li}^* e^{-i\psi_{0i}}) \right] \quad (G-61)$$

2. Incremental solution of the wave equation

By transforming to a coordinate system moving with the wave, the time derivation in the linearized wave equation (G-2) can be eliminated. The linearized wave equation can then be written in the general form

$$\frac{\partial A}{\partial z} = \frac{i}{2k} \nabla_L^2 A - S \quad (G-62)$$

where S is a source term. A separate equation is needed for each transverse component. An incremental solution to (G-62) is

$$\begin{aligned} A(z+\Delta z) &= A(z) + \frac{i\Delta z}{2k} \nabla_L^2 A(z) - \Delta z S \\ &= \left(1 + \frac{i\Delta z}{2k} \nabla_L^2 \right) A(z) - \Delta z S \end{aligned} \quad (G-63)$$

Equation (G-63) is not unitary. An incremental solution to (G-62) which is unitary is

$$A(z+\Delta z) = e^{\frac{i\Delta z}{2k} \nabla_L^2} A(z) - \Delta z S \quad (G-64)$$

Equation (G-64) can be solved in Cartesian coordinates using Fourier transforms. If F is the Fourier transform operator and F^{-1} is its inverse, then

$$\begin{aligned} A(z+\Delta z) &= e^{\frac{i\Delta z}{2k} \nabla_{\perp}^2} F^{-1} F A(z) - \Delta z S \\ &= F^{-1} \left[e^{\frac{i\Delta z}{2k} (k_x^2 + k_y^2)} F A(z) \right] - \Delta z S \end{aligned} \quad (G-65)$$

Using a computer code with fast Fourier transform subroutines, (G-65) can be used to numerically propagate an electromagnetic wave.

The source term S drives the wave and the operator $e^{\frac{i\Delta z}{2k} \nabla_{\perp}^2}$ spreads the wave due to diffraction. To understand why the operator $e^{\frac{i\Delta z}{2k} \nabla_{\perp}^2}$ is used rather than the operator $(1 + \frac{i\Delta z}{2k} \nabla_{\perp}^2)$ of (G-63), we consider the case in which the source term $S = 0$. In this case there can be no gain and the Fourier components $\tilde{A}(k_x, k_y, z) = F A(x, y, z)$ should not vary as a function of z . This property holds for the exponential operator since

$$\left| e^{\frac{i\Delta z}{2k} (k_x^2 + k_y^2)} \right| = 1 \quad (G-66)$$

It is not true, however, for the operator of (G-63). If

$$\tilde{A}(k_x, k_y, z+\Delta z) = \left(1 + \frac{i\Delta z}{2k} (k_x^2 + k_y^2) \right) \tilde{A}(k_x, k_y, z) \quad (G-67)$$

then

$$|\tilde{A}(k_x, k_y, z+\Delta z)|^2 = \left[1 + \left(\frac{\Delta z}{2k} (k_x^2 + k_y^2) \right)^2 \right] |\tilde{A}(k_x, k_y, z)|^2 \quad (G-68)$$

Equation (G-68) says that each mode of the wave will be amplified by a factor $1 + \frac{\Delta z}{2k} (k_x^2 + k_y^2)$ on each iteration of the computer simulation. After many iterations the wave function would be dominated by high frequency noise, since the largest values of k_x and k_y produce the greatest gain.

3. Solution of the wave equation in cylindrical coordinates

The two-stage FEL system we are studying has cylindrical symmetry and cylindrical boundary conditions. It would, therefore, be convenient to model this system in cylindrical coordinates. If we expand $A(\vec{x})$ and $S(\vec{x})$ in terms of their angular Fourier components

$$A(\vec{x}) = \sum_{\lambda=-\infty}^{\infty} a_{\lambda}(r,z) e^{i\lambda\theta} \quad (G-69)$$

and

$$S(\vec{x}) = \sum_{\lambda=-\infty}^{\infty} s_{\lambda}(r,z) e^{i\lambda\theta} \quad (G-70)$$

and substitute these into (G-62) we obtain a series of equations

$$\frac{\partial}{\partial z} a_{\lambda} = \frac{-i}{2k} \left[-\frac{1}{r} \frac{\partial}{\partial r} r \frac{\partial}{\partial r} + \frac{\lambda^2}{r^2} \right] a_{\lambda} - s_{\lambda}. \quad (G-71)$$

The symmetry of the system determines which values of λ are needed to describe the radiation fields. For example, for a cylindrically symmetric system, such as a beam with a Gaussian intensity profile in an open resonator cavity, only the $\lambda=0$ equation would be needed. For a TE_{01} mode in a cylindrical waveguide, only the $\lambda=1$ equation would be needed to describe the wave propagation. We cannot use the fast Fourier transform (FFT) technique with the radial part of the Laplacian to solve the incremental equation as in (G-65). However, it is possible by making a change of variables to reformulate the wave equation in a way that permits the use of fast Fourier transform techniques with cylindrical coordinates. If we define

$$g_{\lambda}(r,z) = \sqrt{r} a_{\lambda}(r,z) \quad (G-72)$$

we find that g satisfies

$$\frac{\partial}{\partial z} g_{\lambda} = \frac{-i}{2k} \left[-\frac{\partial^2}{\partial r^2} + \frac{\lambda^2 - 1/4}{r^2} \right] g_{\lambda} - \sqrt{r} s_{\lambda} \quad (G-73)$$

The incremental solution to this equation is given by

$$g_{\lambda}(r,z+\Delta z) = e^{\frac{-i\Delta z}{2k} \left(-\frac{\partial^2}{\partial r^2} + \frac{\lambda^2 - 1/4}{r^2} \right)} g_{\lambda}(r,z) - \Delta z \sqrt{r} s_{\lambda}(r,z) \quad (G-74)$$

The eigenfunctions of the operator $(-\frac{\partial^2}{\partial r^2} + (\lambda^2 - 1/4)/r^2)$ subject to

the boundary condition $g_\ell(r_{\max}) = 0$ are given by $\sqrt{r} J_\ell(k_{n\ell}r)$ where the J_ℓ 's are ordinary Bessel functions. The $k_{n\ell}$ are determined by the boundary conditions at r_{\max} , that is $J_\ell(k_{n\ell}r_{\max}) = 0$. More precisely

$$\left[-\frac{\partial^2}{\partial r^2} + \frac{(\ell^2 - 1/4)}{r^2} \right] \sqrt{r} J_\ell(k_{n\ell}r) = k_{n\ell}^2 \sqrt{r} J_\ell(k_{n\ell}r) \quad (G-75)$$

In order to utilize the FFT method we rewrite (G-74) in the form

$$g_\ell(r, z+\Delta z) = e^{\frac{i\Delta z}{2k} \frac{(\ell^2 - 1/4)}{r^2}} e^{\frac{i\Delta z}{2k} \frac{\partial^2}{\partial r^2}} g_\ell(r, z) - \Delta z \sqrt{r} s_\ell$$

$$= e^{\frac{-i\Delta z}{2k} V} e^{\frac{-i\Delta z}{2k} P^2} g_\ell(r, z) - \Delta z \sqrt{r} s_\ell \quad (G-76)$$

where the operators P^2 and V are defined by

$$P^2 \equiv -\frac{\partial^2}{\partial r^2} \quad \text{and} \quad V \equiv \frac{\ell^2 - 1/4}{r^2} \quad (G-77, 78)$$

The error resulting from assuming the operators in (G-76) are commutative is of order Δz^2 , which can be made arbitrarily small.

To implement (G-76) we must restrict the radial coordinate to a discrete set of values $r_j = j\Delta r$, where $j=0, 1, \dots, N-1$ and $\Delta r = r_{\max}/N$. We must also sample $g_\ell(r, z)$ at these same points. The operators in the exponentials must also be defined in a discrete way. It was found that defining the discrete operators by

$$P^2 g_\ell(r_j, z) \equiv \frac{[2g_\ell(r_j, z) - g_\ell(r_j + \Delta r, z) - g_\ell(r_j - \Delta r, z)]}{(\Delta r)^2} \quad (G-79)$$

and

$$V g_\ell(r_j, z) = \frac{\ell^2 - 1/4}{r_j^2} g_\ell(r_j, z) \quad (G-80)$$

leads to errors in the numerical solution. This is most easily seen by considering the example in which $\ell=0$ and $a_0=1$ so that $g_0 = \sqrt{r}$. For the continuous operators of (G-77) and (G-78), $(P^2+V)\sqrt{r} = 0$. However, for the discrete operators of (G-79) and (G-80)

$$(P^2+V) g_0(r_j) = \frac{\sqrt{\Delta r}}{(\Delta r)^2} [2\sqrt{j} - \sqrt{j-1} - \sqrt{j+1} - \frac{\sqrt{j}}{4j^2}] \neq 0 \quad (G-81)$$

This inconsistency is most pronounced near the origin where it may cause

serious distortions.

To correct for this problem we modify the operator P^2+V so that the equation

$$[P^2+V] \sqrt{r} J_\ell(k_{n\ell}r) = (k_{n\ell})^2 \sqrt{r} J_\ell(k_{n\ell}r) \quad (G-82)$$

is satisfied exactly when restricted to the discrete r_j and the slowest eigenmode $\sqrt{r} J_\ell(k_{0\ell}r)$. If we retain the definition for P^2 in (G-79), this condition leads to the following set of equations for $V(r_j)$

$$V(r_j) \sqrt{r_j} J_\ell(k_{0\ell}r_j) = (k_{0\ell})^2 \sqrt{r_j} J_\ell(k_{0\ell}r_j)$$

$$- \frac{[2\sqrt{r_j} J_\ell(k_{0\ell}r_j) - \sqrt{r_{j+1}} (k_{0\ell}r_{j+1}) - \sqrt{r_{j-1}} (k_{0\ell}r_{j-1})]}{\Delta r^2} \quad (G-83)$$

The discrete incremental wave equation is now propagated by applying the Fourier transform and its inverse to the system of N equations

$$\begin{aligned} g_\ell(r_j, z+\Delta z) &= e^{\frac{-i\Delta z}{2k}} V(r_j) F^{-1} F \left[e^{\frac{-i\Delta z}{2k}} p^2 g_\ell(r_j, z) \right] - \Delta z \sqrt{r} s_\ell(r_j, z) \\ &= e^{\frac{-i\Delta z}{2k}} V(r_j) F^{-1} \left[e^{\frac{-i\Delta z}{2k}} \frac{2(1-\cos(2\pi j/N))}{(\Delta r)^2} F g_\ell(r_j, z) \right] - \Delta z \sqrt{r} s_\ell(r_j, z) \end{aligned} \quad (G-84)$$

4. Resonant Particle Dynamics in Two-Dimensions

A 2-D computer code has been written to propagate the laser beam using fast Fourier transforms. A number of simplifying assumptions have been made in the code to permit us to quickly obtain useful information about the differences between the one and two dimensional analyses. The code assumes that the pump field is produced by a wiggler magnet and that there is perfect injection of electrons so that the electron transverse canonical momentum equals zero. It is assumed that the transverse

component of the electron velocity is determined entirely by the magnetic field. To study the effect of the applied axial electric field on the resonant phase of the trapped particles we also restrict the electron dynamics to that of the resonant particle. In the resonant particle description, only the trapped electrons contribute to laser gain. The effective transverse current density is therefore

$$\vec{J}_\perp = F_t \frac{J_z}{\beta_z} \vec{\beta}_\perp \quad (G-85)$$

where F_t is the fraction of the electron distribution that is trapped. From (G-54)

$$\vec{\beta}_\perp = - \frac{e\vec{A}}{\gamma mc} = - \frac{e\vec{A}_p}{\gamma mc} \quad (G-86)$$

Using (G-56) and (G-58)

$$\begin{aligned} \vec{J}_\perp \cdot \hat{f}_L^* &= -F_t \frac{J_z}{\beta_z} \frac{e}{\gamma mc} \vec{A}_p \cdot \hat{f}_L^* \\ &= F_t \frac{J_z}{\beta_z} \frac{e}{\gamma mc} A_p^* e^{-i\psi_R} \end{aligned} \quad (G-87)$$

where ψ_R is the phase of the resonant particle. Since the pump field is produced by a wiggler magnet we can choose an initial phase $\phi_p = 0$. Then $A_p = A_p^* = B_m/k_m$, where B_m is the amplitude of the transverse wiggler field and k_m is the wave number. The wave equation (G-60) then becomes

$$\left[\frac{1}{2} \nabla_\perp^2 + i k_L \frac{\partial}{\partial z} \right] A_L e^{i\phi_L} = - \frac{\mu_0 F_t e}{2 \gamma mc} \frac{J_z}{\beta_z} \frac{B_m}{k_m} e^{-i\psi_R} \quad (G-88)$$

From Maxwell's equations

$$\vec{E} = - \frac{\partial \vec{A}}{\partial t} \quad (G-89)$$

Differentiating (G-4) and making the slowly varying amplitude and phase approximations we obtain

$$\frac{\partial \vec{A}_L}{\partial t} = i \omega_L \vec{A}_L \quad (G-90)$$

which when substituted into (G-89) gives

$$\vec{A}_L = \frac{i}{k_L c} \vec{E}_L. \quad (G-91)$$

Using (G-91) in (G-88) we obtain

$$\left[\frac{i}{2k_L} \nabla_L^2 - \frac{\partial}{\partial z} \right] E_L e^{i\phi_L} = - \frac{\mu_0 e}{2} \frac{F_t J_z B_m}{\beta_z k_m} e^{-i\psi_R} \quad (G-92)$$

which is the equation that is solved in the 2-D computer code.

In the code the laser electric field is specified by two column vectors of N elements each, $E_L(r_j)$ and $\phi_L(r_j)$, $j = 0, 1, \dots, N-1$. The source term that produces laser gain is given by the right hand side of (G-92) which is also a column vector with N elements.

To optimize the gain in an FEL amplifier an axial electric field, or alternatively a wiggler taper, could be used. The axial field (or taper) performs two functions. First, it compensates for the phase shift of the ponderomotive wave, produced by the interaction of the electromagnetic field with the electron beam, and second, it determines the value of the resonant phase. In a 1-D model of the FEL the amplitude and the phase of the laser field at a given axial position are uniquely determined and a value of the axial electric field, E_z , can be specified which both compensates for phase shift and produces a desired value of the resonant phase. In a two-dimensional model the electromagnetic field can have different values of amplitude and phase at different radial positions and the amount of phase shift can also vary as a function of radial position.

Since amplitude and phase are no longer uniquely specified, it is only possible to choose one particular radius at which both the phase shift can be compensated and the resonant phase specified. At all other radial positions the resonant phase must be calculated and cannot be chosen a priori. To optimize laser gain a particular radius, r_{opt} , is chosen at which the gain is to be maximized, and a condition is specified for optimizing the gain. One example of such a condition is that the phase space area of the bucket at r_{opt} remain constant along the amplifier.

For simplicity we first consider the case in which phase shift can be neglected. The axial electric field in the amplifier that is needed to produce a particular value of Ψ_R at r_{opt} is given by

$$E(z) = \frac{e E_L(r_{opt}, z) B_m(r_{opt}, z)}{mc k_m \gamma(r_{opt}, z) \beta_z(r_{opt}, z)} \sin \Psi_R(r_{opt}, z) \quad (G-93)$$

It is assumed in (G-93) that $E_z(z)$ is independent of radial position. For the segmented waveguide electrode structure we are considering this is an excellent assumption. With the value of $E(z)$ given in (G-93) the value of the resonant phase at all other radii, r_j , is given by

$$\Psi_R(r_j) = \sin^{-1} \left[\frac{mck_m}{e} \gamma(r_j) \beta_z(r_j) \frac{E_z}{E_L(r_j) B_m(r_j)} \right], \quad (G-94)$$

where the z dependence of the quantities in (G-94) has not been shown explicitly.

All of the quantities in (G-94) are either constants or have a slow radial dependence, except for E_L and Ψ_R . Therefore,

$$\sin \Psi_R(r_j) \propto \frac{1}{E_L(r_j)} \quad (G-95)$$

Now in the resonant particle model, laser gain is proportional to $\sin \Psi_R$ times the fraction of the electrons trapped in the bucket. If we assume the phase space buckets are filled with particles, then the fraction trapped will be proportional to bucket area. Bucket area is proportional to the quantity $E_L^{1/2} \eta(\Psi_R)$ where $\eta(\Psi_R)$ is the ratio of the area of a bucket of resonant phase Ψ_R to the area of a bucket of resonant phase $\Psi_R=0$. Making these assumptions

$$\frac{\partial E_L}{\partial z} = E_L^{1/2} \eta(\Psi_R) \sin \Psi_R = \frac{\eta(\Psi_R)}{E_L^{1/2}} \quad (G-96)$$

If the resonant phase $\Psi_R(r_j) = 90^\circ$, the bucket area will equal zero and there will be no gain. From (G-95) this means that laser gain will decrease to zero for

$$E_L(r_j) < E_L(r_{opt}) \sin \Psi_R(r_{opt}) \quad (G-97)$$

This is shown in Figure 17 in which a resonant phase angle of 24° was chosen at r_{opt} .

VARIATION OF LASER GAIN ACROSS A BEAM
AS A FUNCTION OF LASER INTENSITY

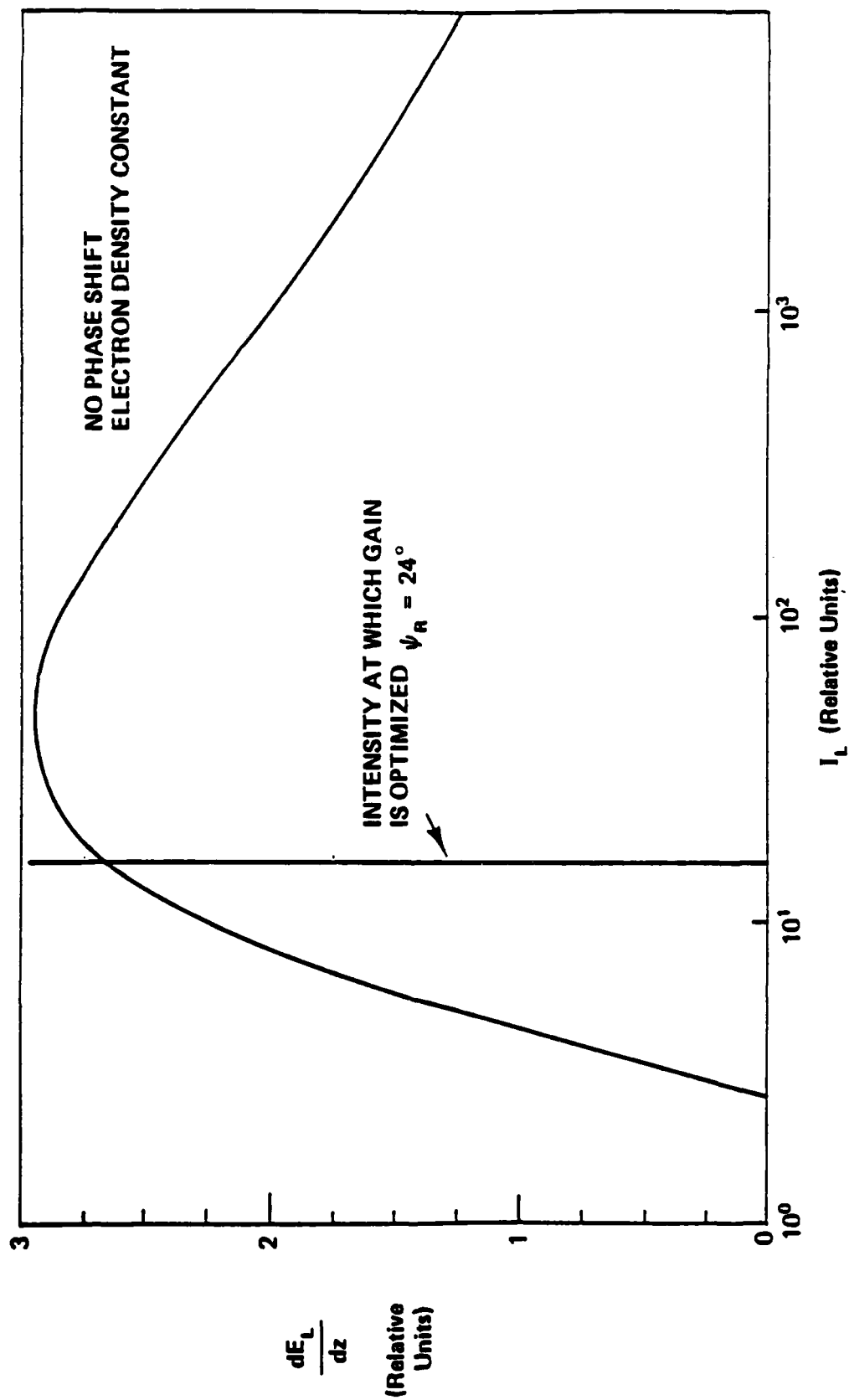


Figure 17

If the phase shift is taken into consideration then both the amplitude and phase of the laser beam will vary as a function of radius and the formula that determines the axial field needed to produce a given resonant phase at r_{opt} is more complicated than (G-93). If a phase shift of $\Delta\phi(r_{opt})$ occurs at r_{opt} over a distance Δz , the effect of this shift can be negated by accelerating or decelerating the electrons over the interval Δz so that the electron distribution remains in the same position relative to the bucket. The desired value of the resonant phase $\Psi_R(r_{opt})$ is then produced by adding to the field required to compensate for phase shift an additional amount equal to the field needed to produce the desired resonant phase in the absence of phase shift. The resultant value of E_z is then given by

$$E_z = \frac{e E_L B_m}{\gamma m c k_m \beta_z} \sin \Psi_R + \frac{\gamma m c^2}{e \Delta z} \left[\frac{-2\gamma^2}{(1+\alpha^2)(k_L+k_m)} \frac{\Delta\phi}{\Delta z} + \frac{\gamma_0^2 - \gamma^2}{\gamma_0^2} \right] \quad (G-98)$$

where all terms are evaluated at r_{opt} . γ_0 is the initial value of the resonant energy at the input end of the amplifier and

$$\alpha = \frac{e B_m}{m c k_m} \quad (G-99)$$

at radii other than r_{opt} the phase shift will in general be different than $\Delta\phi(r_{opt})$. The resonant phase at $r_j \neq r_{opt}$ can be determined by first finding the electric field required to compensate for phase shift, E' .

The electric field ΔE_z that remains after E' is subtracted from E_z can then be substituted for E_z in (G-94) to obtain the resonant phases at $r_j \neq r_{opt}$.

$$\Delta E(r_j) = E_z - E'(r_j) \quad (G-100)$$

$$\Psi_R(r_j) = \sin^{-1} \left[\frac{m c k_m}{e} \gamma(r_j) \beta_z(r_j) \frac{\Delta E_z(r_j)}{E_L(r_j) B_m(r_j)} \right] \quad (G-101)$$

H. References

1. S. Mani, W.J. Schafer Associates, Report No. WJSA-FTR-82-193, "Low Voltage FEL Optics", March 5, 1982.
2. J.A. Stratton, Electromagnetic Theory, McGraw Hill, New York (1941).
3. M. Born and E. Wolf, Principles of Optics, McMillan, New York (1964).
4. E. Hagen and H. Rubens, Ann. d. Physik 11, 873 (1903).
5. T. Moreno, Microwave Transmission Design Data, Dover, New York (1958).
6. L.R. Elias and J.M. Madey, Rev. Sci. Inst. 50, 1335 (1979).
7. K. Halbach, Nucl. Inst. and Meth. 169, 1 (1980).
8. K. Halbach, Nucl. Inst. and Meth. 187, 109 (1981).
9. R.F. Holsinger, "The Drift Tube and Beam Line Quadrupole Permanent Magnets for the NEN Proton Linac", Proc. of the Linear Accel. Conf., Montauk, Long Island, Sept. 1979.
10. L.R. Elias and G. Ramian, "Design of the UCSB FEL Electron Beam System", UCSB Report No. QIFEL 011/81 (1981).

I. Distribution List

Director
Defense Advanced Research Projects
Agency
(3 copies)
Attn: Technical Library
1400 Wilson Boulevard
Arlington, VA 22209

Office of Naval Research
(3 copies)
Physics Division Office (Code 412)
800 North Quincy Street
Arlington, VA 22217

Office of Naval Research
Director, Technology (Code 200)
800 North Quincy Street
Arlington, VA 22217

Naval Research Laboratory
(3 copies)
Department of Navy
Attn: Technical Library
Washington, DC 20375

Office of the Director of Defense
Research and Engineering
(3 copies)
Information Office Library Branch
The Pentagon
Washington, DC 20301

U.S. Army Research Office
(2 copies)
Box 1211
Research Triangle Park, NC 27709

Defense Technical Information Center
(12 copies)
Cameron Station
Alexandria, VA 22314

Director, National Bureau of Standards
Attn: Technical Library
Washington, DC 20234

Commanding Officer
(3 copies)
Office of Naval Research Western
Detachment Office
1030 East Green Street
Pasadena, CA 91101

Commanding Officer
(3 copies)
Office of Naval Research
Eastern/Central Detachment Office
495 Summer Street
Boston, MA 02210

Commandant of the Marine Corps
Scientific Advisor (Code RD-1)
Washington, DC 20380

Naval Ordnance Station
Technical Library
Indian Head, MD 20640

Naval Postgraduate School
Technical Library (Code 5632.2)
Point Mugu, CA 93010

Naval Ordnance Station
Technical Library
Louisville, KY 40214

Commanding Officer
Naval Ocean Research & Development
Activity
Technical Library
NSTL Station, MS 39529

Naval Explosive Ordnance Disposal
Facility
Technical Library
Indian Head, MD 20640

Naval Ocean Systems Center
Technical Library
San Diego, CA 92152

Naval Surface Weapons Center
Technical Library
Silver Springs, MD 20910

Naval Ship Research & Development
Center
Central Library (Code L42 and L43)
Bethesda, MD 20084

Naval Avionics Facility
Technical Library
Indianapolis, IN 46218

KMS Fusion, Inc.
3621 South State Road
P.O. Box 1567
Ann Arbor, MI 48106

Stephen B. Segall
Dr. H. Rodney Hiddleston
Dr. H. Takeda
Dr. Scott Van Laven
Dr. Jon T. Larsen
Dr. Alexander J. Glass

Dr. R. Barbini
INFN
Frascati, Italy

Dr. Robert Behringer
Office of Naval Research
1030 Green Street
Pasadena, CA 91106

Dr. Charles Brau
Applied Photochemistry Division
Los Alamos National Scientific
Laboratory
P. O. Box 1163, M.S. 816
Los Alamos, NM 87545

Dr. Maria Caponi
TRW
One Space Park Drive
Redondo Beach, CA 90278

Dr. William Colson
Quantum Institute
University of California
Santa Barbara, CA 93106

Dr. D. A. G. Deacon
HEPL
Stanford University
Stanford, CA 94305

Professor P. Diamant
Columbia University
Department of Electrical Engineering
New York, NY 10027

Dr. Luis Elias
Quantum Institute
University of California
Santa Barbara, CA 93106

Pierre Elleaume
L.U.R.E.
University of Paris
Orsay, France

Dr. Jim Elliot
X-Division, MS 531
Los Alamos National Scientific
Laboratory
Los Alamos, NM 87545

Dr. Barry J. Feldman
AFOSR
Bolling AFB
Washington, D.C. 20332

Dr. Roger Freedman
Quantum Institute
University of California
Santa Barbara, CA 93106

Dr. A. Fruchtman
Center for Plasma Physics
Racah Institute of Physics
Hebrew University
Jerusalem, Israel

Dr. Juan Gallardo
Quantum Institute
University of California
Santa Barbara, CA 93106

Dr. A. T. Georges
444 S. Kingsley Drive
Los Angeles, CA 90020

Dr. John C. Goldstein, X-1
Los Alamos National Scientific
Laboratory
P.O. Box 1163
Los Alamos, NM 87545

Dr. Yehuda Goren
Scientific Department
Ministry of Defense
P.O. Box 2250
Haifa, Israel 31021

Dr. Avraham Gover
School of Engineering
Tel Aviv University
Tel Aviv, Israel

Dr. J. L. Hirshfield
Yale University
Mason Laboratory
400 Temple Street
New Haven, CT

Mr. Ronald F. Holsinger
Field Effects Corp.
27 Old East Street
Carlisle, MA 01741

Dr. Fred Hopf
Optical Sciences Center
University of Arizona
Tucson, AZ 85721

Dr. S. F. Jacobs
Optical Sciences Center
University of Arizona
Tucson, AZ 85721

Dr. Alfredo Luccio
Brookhaven National Laboratory
Accelerator Department
Upton, NY 11975

Dr. John Madey
Physics Department
Stanford University
Stanford, CA 94305

Dr. Joseph Mangano
DARPA
1400 Wilson Boulevard
Arlington, VA 22209

Dr. Siva A. Mani
W. J. Shafer Associates, Inc.
10 Lakeside Office Park
Wakefield, MA 01880

Dr. T. C. Marshall
Applied Physics
Columbia University
New York, NY 10027

Dr. Gerald T. Moore
Department of Physics
University of Mexico
Albuquerque, NM

Dr. Philip A. Morton
SLAC
P.O. Box 4349
Stanford, CA 94305

Dr. George Neil
TRW
One Space Park
Redondo Beach CA 90278

Dr. Brian Newnam
MS J564
Los Alamos National Scientific
Laboratory
P.O. Box 1663
Los Alamos, NM 87545

Dr. Kelvin Neil
Lawrence Livermore National
Laboratory
Code L-321, P.O. Box 808
Livermore, CA 94550

Dr. Richard Pantell
Stanford University
Stanford, CA 94305

Dr. Claudio Pellegrini
Brookhaven National Laboratory
Associated Universities, Inc.
Upton, L.I., NY 11973

Dr. Alan Pike
DARPA
1400 Wilson Boulevard
Arlington, VA 22209

Dr. Hersch Pilloff
Code 421
Office of Naval Research
Arlington, VA 22217

Dr. Don Prosnitz
Lawrence Livermore National
Laboratory
Livermore, CA 94550

Mr. Gerald Ramian
Quantum Institute
University of California
Santa Barbara, CA 93106

Dr. Alberto Renieri
CNEA
Frascati, Italy 00044

Dr. John L. Richardson
Department of Electrical and
Computer Engineering
University of California
Santa Barbara, CA 93106

Dr. Helmut Wiedeman
SLAC
Stanford, CA 94305

Professor S. P. Schlesinger
Columbia University
Department of Electrical Engineering
New York, NY 10027

Dr. Marvin O. Scully
Department of Physics
University of Mexico
Albuquerque, NM

Dr. Earl D. Shaw
Bell Labs
600 Mountain Avenue
Murray Hill, NJ 07974

Dr. Chun-Ching Shih
TRW
One Space Park
Redondo Beach, CA 90278

Dr. Jack Slater
Mathematical Sciences, NW
P.O. Box 1887
Bellevue, WA 98009

Mr. Todd Smith
Hansen Labs
Stanford University
Stanford, CA 94305

Dr. Phil Sprangle
Naval Research Laboratory
Washington, D.C. 20375

Dr. Abraham Szoke
Lawrence Livermore National
Laboratory
MS/L-470, P.O. Box 808
Livermore, CA 94550

Dr. Cha-Mei Tang
Naval Research Laboratory
Washington, D.C. 20375

Dr. John Ward
Physics Department
University of Michigan
Ann Arbor, MI 48109